Manuscript prepared for Atmos. Chem. Phys.
with version 1.3 of the LaTeX class copernicus.cls.
Date: 9 September 2015

How consistent are top-down hydrocarbon emissions based on formaldehyde observations from GOME-2 and OMI?

T. Stavrakou[1], J.-F. Müller[1], M. Bauwens[1], I. De Smedt[1], M. Van Roozendael[1], M. De Mazière[1], C. Vigouroux[1], F. Hendrick[1], M. George[2], C. Clerbaux[2,3], P.-F. Coheur[3], and A. Guenther[4]

[1]Belgian Institute for Space Aeronomy, Avenue Circulaire 3, 1180, Brussels, Belgium
[2]UPMC Univ. Paris 6; Université Versailles St.-Quentin; CNRS/INSU, LATMOS-IPSL, 75252, Cedex 05, Paris, France
[3]Spectroscopie de l'Atmosphère, Service de Chimie Quantique et Photophysique, Université Libre de Bruxelles, 1050, Belgium
[4]Atmospheric Sciences and Global Change Division, Pacific Northwest National Laboratory, Richland, Washington State, USA

Abstract.

The vertical columns of formaldehyde (HCHO) retrieved from two satellite instruments, the Global Ozone Monitoring Instrument-2 (GOME-2) on Metop-A and the Ozone Monitoring Instrument (OMI) on Aura, are used to constrain global emissions of HCHO precursors from open fires, vegetation and human activities in the year 2010. To this end, the emissions are varied and optimized using the adjoint model technique in the IMAGESv2 global CTM (chemistry-transport model) on a monthly basis and at the model resolution. Given the different local overpass times of GOME-2 (9h30) and OMI (13h30), the simulated diurnal cycle of HCHO columns is investigated and evaluated against ground-based optical measurements at 7 sites in Europe, China and Africa. The modelled diurnal cycle exhibits large variability, reflecting competition between photochemistry and emission variations, with noon or early afternoon maxima at remote locations (oceans) and in regions dominated by anthropogenic emissions, late afternoon or evening maxima over fire scenes, and midday minima in isoprene-rich regions. The agreement between simulated and ground-based columns is generally better in summer (with a clear afternoon maximum at mid-latitude sites) than in winter, and the annually averaged ratio of afternoon to morning columns is slightly higher in the model (1.126) than in the ground-based measurements (1.043).

The anthropogenic VOC (volatile organic compound) sources are found to be weakly constrained by the inversions on the global scale, mainly owing to their generally minor contribution to the HCHO columns, except over strongly polluted regions, like China. The OMI-based inversion yields total flux estimates over China close to the bottom-up inventory (24.6 vs. 25.5 TgVOC/yr in the a priori) with, however, pronounced increases in the Northeast China and reductions in the south. Lower fluxes are estimated based on GOME-2 HCHO columns (20.6 TgVOC/yr), in particular over the Northeast, likely reflecting mismatches between the observed and the modelled diurnal cycle in this region.

The resulting biogenic and pyrogenic flux estimates from both optimizations generally show a good degree of consistency. A reduction of the global annual biogenic emissions of isoprene is derived, by 9% and by 13% according to GOME-2 and OMI, respectively, compared to the a priori estimate of 363 Tg in 2010. The reduction is largest (up to 25-40%) in the Southeastern US, in accordance with earlier studies. The GOME-2 and OMI satellite columns suggest a global pyrogenic flux decrease by 36% and 33%, respectively, compared to the GFEDv3 inventory. This decrease is especially pronounced over tropical forests such as Amazonia and Thailand/Myanmar, and is supported by comparisons with CO observations from IASI (Infrared Atmospheric Sounding Interferometer). In contrast to these flux reductions, the emissions due to harvest waste burning are strongly enhanced in the Northeastern China plain in June (by ca. 70% in June according to OMI) as well as over Indochina in March. Sensi-

Correspondence to: T. Stavrakou (jenny@aeronomie.be)

tivity inversions showed robustness of the inferred estimates, which were found to lie within 7% of the standard inversion results at the global scale.

---

1 Introduction

Besides a small direct source, the dominant source of formaldehyde (HCHO) is its photochemical formation due to the oxidation of methane and non-methane volatile organic compounds (NMVOCs) emitted by the biosphere, vegetation fires and human activities. Methane oxidation is by far the largest contributor to the HCHO formation (ca. 60% on the global scale), while the remainder is due to oxidation of a large variety of VOCs of anthropogenic, pyrogenic and biogenic origin (Stavrakou et al., 2009a). The main removal processes (Sander et al., 2011) are the oxidation by OH,

$$HCHO + OH (+ O_2) \rightarrow CO + HO_2 + H_2O,$$

ultimately producing CO and converting OH to HO_2, and photolysis reactions

$$HCHO + h\nu \rightarrow CO + H_2, \text{ and}$$

$$HCHO + h\nu (+ 2\ O_2) \rightarrow CO + 2\ HO_2,$$

producing CO, H_2 as well as HO_2 radicals.

Because of its short photochemical lifetime (ca. 4-5 hours), and of the short lifetime of its main NMVOC precursors, most importantly isoprene, enhanced levels of HCHO are directly associated with the presence of nearby hydrocarbon emission sources. Relying on the measurement of HCHO column densities from space by solar backscatter radiation in the UV-Visible spectral region (Chance et al., 2000; De Smedt et al., 2008, 2012; Hewson et al., 2013; De Smedt et al., 2015; González Abad et al., 2015), the use of HCHO measurements to inform about the VOC precursor fluxes was explored through a large body of literature studies. The first studies focused on the derivation of isoprene fluxes in the U.S. constrained by HCHO columns from GOME or OMI instruments (Palmer et al., 2003, 2006; Millet et al., 2006, 2008). The estimation of isoprene emissions was extended to cover other regions, e.g. South America (Barkley et al., 2008, 2009) and Africa (Marais et al., 2012, 2014), with special efforts to exclude satellite scenes affected by biomass burning, and Europe (Dufour et al., 2009). Fu et al. (2007) reported top-down isoprene and anthropogenic reactive VOCs fluxes over East and South Asia, and more recently anthropogenic emissions of reactive VOCs in eastern Texas were estimated using the oversampling technique applied to OMI HCHO observations (Zhu et al., 2015). Based on SCIAMACHY observations, space-based emissions of isoprene and pyrogenic NMVOCs were derived on the global scale using the adjoint model approach (Stavrakou et al., 2009b,c). Each of those studies was constrained by one satellite dataset, and in many cases, conflicting answers were found regarding the magnitude and/or spatiotemporal variability of the underlying VOC sources, mostly owing to differences in the satellite column products, in the models used to infer top-down estimates, and in the emission inventories used as input in the models. The latter point is very often a source of confusion, since a very large range of estimates can be obtained using the same emission model depending on the choice of input variables. Indeed, the isoprene fluxes estimated using MEGAN (Guenther et al., 2006), the most commonly used bottom-up emission model for biospheric emissions, vary strongly depending on the driving variables used (e.g. meteorology, landcover), leading to an uncertainty of about a factor of 5 for the global isoprene emissions (Arneth et al., 2011) and underscoring the need for clearly indicated a priori emission information in order to allow meaningful comparisons between different studies.

Despite significant progress in the field, the derivation of VOC emissions using HCHO columns remains challenging, mainly owing to the large number and diversity of HCHO precursors, to uncertainties regarding their sources and speciation profiles, and to inadequate or incomplete knowledge of their chemical mechanisms and pathways leading to HCHO formation. In addition, it crucially depends on the quality of the satellite retrievals, and therefore efforts to address aspects such as instrumental degradation, temporal stability of the retrievals, noise reduction, and error characterization are of primary importance (De Smedt et al., 2012, 2015; Hewson et al., 2013; González Abad et al., 2015).

The advent of new satellites measuring at different overpass times, like GOME-2, SCIAMACHY and OMI, opens new avenues in the derivation of top-down estimates. However, it also raises new questions regarding the consistency of the estimated fluxes from different instruments. Indeed, a recent study focusing on Tropical South America reported a factor of 2 difference between the SCIAMACHY- and OMI-based isoprene fluxes derived using the same model, a difference which apparently could not be explained by differences in the sampling features of the sensors or by uncertainties in the air mass factor calculations, and which might be partly due to model deficiencies pertaining to the diurnal cycle of the HCHO columns (Barkley et al., 2013).

The main objective of this study is therefore to address the issue of consistency between global VOC flux strengths inferred from one complete year of GOME-2 and OMI HCHO column densities, taking into account their different overpass times. Field campaign measurements show that the diurnal patterns of surface HCHO concentrations are mostly influenced by the magnitude and diurnal variability of precursor emissions and the development of the boundary layer. A midday peak followed by gradual decrease in the evening concentrations were observed at a tropical forest in Borneo (MacDonald et al., 2012), whereas HCHO concentration peaked in the evening during cool days and around midday in warm and sunny conditions at a forest site in California (Choi et al., 2010) and near a city location in the Po valley (Junkermann, 2009). Long-term diurnal measurements of HCHO columns are limited, but are less influenced by variations in boundary layer mixing and are directly comparable with the satellite observations. Here, we investigate first the diurnal variability of HCHO columns simulated by the IMAGESv2 global CTM, and evaluate the model skill to reproduce the observed diurnal cycle of HCHO columns at seven different locations in Europe, China, and tropical regions.

Retrieved HCHO columns from GOME-2 and OMI, with local overpass times 9h30 and 13h30, respectively, are used to constrain the VOC emissions. The algorithms developed for the two sensors were designed to ensure the maximum consistency between the two sets of observations, as described in detail in De Smedt et al. (2015). The top-down emission estimates are derived using an inversion framework based on the adjoint of the IMAGESv2 CTM (Müller and Stavrakou, 2005; Stavrakou et al., 2009a) and fluxes are optimized per month, model grid and emission category (anthropogenic, biogenic and pyrogenic). The same inversion setup is applied using either GOME-2 or OMI measurements as top-down constraints for 2010, a particularly warm and dry year with intense fires and enhanced biogenic emissions. Sensitivity studies are carried out to assess the robustness of the findings to different assumptions, e.g. to changes of the prescribed a priori errors on the emission fluxes in the inversion.

In Sect. 2 the IMAGESv2 model is briefly described and the HCHO budget is discussed, whereas the formation of HCHO in the oxidation of anthropogenic VOCs is presented in detail in the Supplement. The modelled and observed diurnal cycle of HCHO columns is discussed in Sect. 3. The satellite HCHO columns used to constrain the inversions and the inversion methodology are presented in Sect. 4 and 5. An overview of the results inferred from the inversions using GOME-2 and OMI data and global results from sensitivity case studies are presented in Sect. 6. The VOC emissions inferred at the mid-latitudes (North America, China) and in tropical regions (Amazonia, Indonesia, Indochina, Africa) are thoroughly described in Sect. 7 and 8. Finally, conclusions are drawn in Sect. 9.

2 HCHO simulated with IMAGESv2

The IMAGESv2 global CTM is run at $2^\circ \times 2.5^\circ$ horizontal resolution and extends vertically from the Earth's surface to the lower stratosphere through 40 unevenly spaced sigma-pressure levels. It calculates daily averaged concentrations of 131 transported and 41 short-lived trace gases with a time step of 6 hours. Meteorological fields are obtained from ERA-Interim analyses of the European Centre of Medium-Range Weather Forecasts (ECMWF). Advection is driven by monthly averaged winds, while the effect of wind temporal variability at time scales shorter than one month is represented as horizontal diffusion (Müller and Brasseur, 1995). Convection is parameterized based on daily ERA-Interim updraft mass fluxes. Turbulent mixing in the planetary boundary layer uses daily diffusivities also obtained from ERA-Interim. Rain and cloud fields (and therefore also the photolysis and wet scavenging rates) are also based on daily ERA-Interim fields. The effect of diurnal variations are considered through correction factors on the photolysis and kinetic rates obtained from model simulations accounting for the diurnal cycle of photorates, emissions, convection and boundary layer mixing (Stavrakou et al., 2009a). A thorough model description is given in Stavrakou et al. (2013) and references therein. The target year of this study is 2010.

Anthropogenic emissions are obtained from the RETRO 2000 database (http://retro.enes/org, Schultz et al. (2008)), except over Asia where the REASv2 inventory for year 2008 is used (Kurokawa et al., 2013). The diurnal profile of anthropogenic emissions follows Jenkin et al. (2000). Isoprene emissions (including their diurnal, day-to-day and seasonal variations) are obtained from the MEGAN-MOHYCAN-v2 inventory (http://tropo.aeronomie.be/models/isoprene.htm, Müller et al. (2008); Stavrakou et al. (2014)) and are estimated at 363 Tg in 2010 (Fig. 1). Monthly averaged biogenic methanol emissions ($\sim$100 Tg/year globally) are taken from a previous inverse modelling study (Stavrakou et al., 2011) using IMAGESv2 and methanol total columns from IASI. Biogenic emissions of acetaldehyde (22 Tg/year) and ethanol (22 Tg/year) are calculated following Millet et al. (2010). The model also includes the biogenic emissions of ethene, propene, formaldehyde, acetone and monoterpenes from MEGANv2 (http://eccad.sedoo.fr). Note that the non-isoprene biogenic VOC emissions are not varied in the source inversions.

Open vegetation fire emissions are taken from GFEDv3 (van der Werf et al., 2010), with emission factors for tropical, extratropical, savanna and peat fire burning provided from the 2011 update of the recommendations by Andreae and Merlet (2001). The GFEDv3 emission is estimated at 105.4 TgVOC in 2010, equivalent to 2.26 Tmoles (average molecular weight of 46.5 kg/kmol) (Fig. 1). The diurnal profile of biomass burning emissions was derived based on a complete year of geostationary active fires and fire radiative power observations from the SEVIRI imager over Africa (Roberts et al., 2009). The analysis of the fire cycle, performed over 20 different land cover types in the Northern and Southern Hemisphere Africa, exhibits strong diurnal variability and very similar patterns in both hemispheres. According to this dataset, fire activity is negligible during the night and low in the early morning, it peaks around 13h30 local time, and decreases rapidly in the afternoon hours. This profile is in fairly good agreement with the averaged diurnal cycle of active fire observations constructed from the GOES geostationary satellite encompassing North, Central and South America (Mu et al., 2011), and therefore it is applied to all fires worldwide. Note, however, that this specific temporal profile might not be appropriate for some locations, e.g. peat fires over Russia.

The vertical profiles of pyrogenic emissions are taken from a new global dataset (Sofiev et al., 2013) of vertical smoke profiles from open fires, based on plume top heights computed by a semi-empirical model (Sofiev et al., 2012), and fire radiative power from the MODIS instrument. These profiles are highly variable depending on the season and the year. Forest regions are characterized by high altitude plumes (up to 6-8 km), whereas grasslands generally emit within 2-3 km. About half of emitted flux is injected within the boundary layer. The 5^{th}, median, 80^{th} and 99^{th} monthly percentiles of injection profiles maps of this dataset were obtained from the GlobEmission website (http://www.globemission.eu) and implemented in the CTM.

The chemical mechanism of isoprene oxidation accounts for OH recycling according to the Leuven Isoprene mechanism LIM0 (Peeters et al. (2009); Peeters and Müller (2010); Stavrakou et al. (2010)), and its upgraded version LIM1 (Peeters et al., 2014). LIM1 is based on a theoretical reevaluation of the kinetics of isoprene peroxy radicals undergoing 1,5 and 1,6-shift isomerization, and is in satisfactory agreement (factor of $\sim$2) with experimental yields of the hydroperoxy aldehydes (HPALDs) believed to be major isomerization products (Crounse et al., 2011). Based on box model calculations using the Kinetic PreProcessor (KPP) chemical solver (Damian et al., 2002), the isomerization of isoprene peroxy radicals is estimated to decrease the molar HCHO yield by $\sim$8% in high NOx conditions (2.39 vs. 2.60 mol/mol after two months of simulation at 1 ppbv NO_2), and by $\sim$15% in low NOx conditions (1.91 vs. 2.25 after two months at 0.1 ppbv NO_2). These estimated changes are however very uncertain, given their dependence on the unimolecular reaction rates of isoprene peroxy radicals and on the poorly constrained fate of the isomerization products.

The speciation profile for anthropogenic NMVOC emissions is based on the UK National Atmospheric Emissions Inventory (NAEI, Goodwin et al. (2001)). According to

NAEI, 49 (out of the 650 considered) compounds account for ca. 81% of the total UK emission, 17 out of them are explicitly accounted for in IMAGESv2, while a lumped compound OAHC (other anthropogenic hydrocarbons) accounts for the remaining 32 species. The chemical mechanism of OAHC is adapted in order to reproduce the yields of HCHO from the mix of 32 higher NMVOCs. This is realized based on time-dependent box model calculations using the semi-explicit Master Chemical Mechanism (MCMv3.2, http://mcm.leeds.ac.uk/MCM/, Saunders et al. (2003); Bloss et al. (2005)). Details are given in the Supplement.

Based on IMAGESv2 model simulations, the global annual HCHO budget is estimated at 1600 Tg HCHO and is dominated by photochemical production, whereas less than 1% is due to direct emissions. The most important source of HCHO is methane oxidation (60% globally), the remainder being due to the oxidation of biogenic (30%), anthropogenic (7%) and pyrogenic (3%) hydrocarbons (Stavrakou et al., 2009a). The main removal process is photolysis, which accounts for 70% of the global sink, followed by OH oxidation (26%), and by dry and wet deposition. The aforementioned production and loss processes result in a global lifetime of 4.6 hours.

3 Diurnal cycle of HCHO columns

3.1 Model processes and sensitivity

The top-down determination of VOC emissions based on GOME-2 and OMI data assumes that the model reproduces reasonably well the diurnal cycle of HCHO columns. To test this assumption would require a large number of well distributed ground-based observations, which are however scarce and intermittent. We present further below a comparison with a limited dataset of column observations at surface sites, most of which are located at or near pollution centers at mid-latitudes. In order to better characterize the diurnal cycle and to identify the factors influencing it in the model, we present in Fig. 2 the modelled diurnal variations of HCHO columns at selected locations, and in Fig. 3 the distribution of the local time of the maximum in the diurnal cycle of HCHO columns. Fig. 2 also diplays the results of sensitivity calculations described in Table 1, which neglect either the diurnal cycle of emissions (NDC) or the biomass burning emissions (NBB), in comparison to the standard model results. The results of additional sensitivity simulations related to vertical transport (Table 1) are not shown here for clarity.

A striking feature of Fig. 2 and Fig. 3 is the large diversity of diurnal profiles accross the seasons and locations. Very little HCHO variations are seen at high latitudes during the winter, due to the very low photochemical activity and absence of notable emissions. In regions where anthropogenic emissions are the dominant source of HCHO precursors, such as Northwestern Europe, Eastern China, India and the Middle East (Fig. 1), the diurnal cycle displays a midday maximum and a minimum at the end of the night (Fig. 2, S. England and Fig. 3). As can be seen in Fig. 2, the diurnal cycle of anthropogenic emissions has a very small impact at these locations. This is due to the fairly long photochemical lifetimes of most anthropogenic NMVOCs. Their relatively low short-term HCHO yields in comparison with the final yields (see Table 1) implies that most HCHO formation occurs days after the precursor has been emitted. The midday maximum therefore reflects the diurnal cycle of OH concentrations, very low at night and maximum when radiation is highest (Logan et al., 1981).

Over the Eastern US, the wintertime (November to March) diurnal cycle displays a similar pattern due to anthropogenic emissions. In the summer, however, when biogenic isoprene is the dominant VOC, a completely different behavior is predicted, with a noon minimum and a maximum in the evening or even in the early morning (Fig. 2, Arkansas and Fig. 3). A relatively similar pattern is found in the Manaus region in the Amazon in July-September (Fig. 2), in agreement with a previous modelling study using GEOS-Chem and focussing on Amazonia (Barkley et al., 2011). At all sites impacted by isoprene (Arkansas, Borneo, Manaus and Mato Grosso), the simulation neglecting diurnal variations of emissions (Fig. 2, NDC, blue curve) leads to a continuous HCHO buildup during the night and to a pronounced morning maximum followed by a gradual decrease during daytime until a minimum in late afternoon or early evening. The nighttime buildup in that simulation follows the slow isoprene oxidation (mostly by ozone) and the near-absence of HCHO sinks, whereas the gradual HCHO decrease during the day reflects the decline of the accumulated isoprene and intermediate oxidation products due to OH oxidation. Although the daytime chemical lifetime of isoprene is short (less than 1 hour at an OH concentration of $4{\cdot}10^6$ molec.cm^{-3}), a large fraction of the formaldehyde production due to isoprene involves longer-lived intermediates (such as methylvinylketone, methacrolein, hydroxyacetone, hydroperoxides, etc.) resulting in a delayed formaldehyde production.

When the diurnal cycle of isoprene emissions is taken into account (Fig. 2, STD, red curve), the midday emission maximum leads to a HCHO minimum and to an increase afterwards, due to the delayed production from isoprene (Arkansas, Manaus and Mato Grosso). It has been pointed out (Barkley et al., 2011) that the nighttime HCHO accumulation and morning maximum near Manaus in September might be unrealistic, as models are often unable to reproduce the observed rapid decline of isoprene concentrations during the evening at different surface sites. Nighttime chemistry, deposition and boundary layer processes might indeed be poorly represented in models, causing significant deviations from the patterns described above. As is obvious from Figs. 2 and 3, different locations or seasons display often very different diurnal patterns, for complex reasons including radiation and NOx levels, the occurrence of biomass burning, mixing processes, etc. Note however, that sensitivity simulations neglecting the diurnal cycle of boundary layer mixing and deep convection fluxes were found to cause only minimal deviations from the columns of the standard model calculations.

Vegetation fires are found to cause locally very strong variations with maximum values in the evening, exceeding by up to 70% the morning minimum value (Central Alaska in May and July, Mato Grosso in September). As seen in Fig. 3, strong emissions over Eastern Siberia, European Russia, Central Canada, Angola, Brazil and Northern Australia are most often associated with HCHO column maxima in the late afternoon and evening.

3.2 Model evaluation

To evaluate the diurnal cycle of the modelled HCHO column, we use ground-based remote-sensed measurements at the 7 following sites :

1. Cabauw/The Netherlands (52°N, 5° E), 8 June – 21 July 2009 (Pinardi et al., 2013)
2. Observatoire de Haute Provence (OHP)/France (43.94°N, 5.71°E), 26 June 2007 – 20 March 2013 (Valks et al., 2011)
3. Uccle/Belgium (50.78°N, 4.35°E), 1 May 2011 – 23 April 2012 (Gielen et al., 2014)
4. Beijing/China (39.98°N, 116.38°E), 3 July 2008 – 17 April 2009 (Vlemmix et al. (2015), see also Hendrick et al. (2014))
5. Xianghe/China (39.75°N, 116.96°E), 7 March 2010 – 26 December 2013 (Vlemmix et al. (2015), see also Hendrick et al. (2014))
6. Bujumbura/Burundi (3°S, 29°E), 25 November 2013 – 22 January 2014 (De Smedt et al., 2015)
7. Reunion Island/France (20.9°S, 55.5°E), 1 August 2004 – 25 October 2004, 21 May 2007 – 15 October 2007, 2 June 2009 – 28 December 2009, and 11 January 2010 – 16 December 2010 (Vigouroux et al., 2009).

The MAX-DOAS (Multi-axis differential optical absorption spectroscopy) technique (Hönninger et al., 2004; Platt and Stutz, 2008) was used in all cases, except at Reunion Island where the FTIR (Fourier Transform infrared spectroscopy) technique is used (Griffiths and de Haseth, 2007; Vigouroux et al., 2009). Total HCHO columns are measured at all stations, and profiles are also measured at Beijing, Xianghe, and Bujumbura.

Figures 4 and 5 illustrate the diurnal cycle of observed and modelled HCHO columns seasonally averaged and normalized by their noon values. The ratio of the observed columns at 13h30 and 9h30 ranges mostly between 0.8 and 1.2, although values close to 1.4 are found at one site (OHP). The modelled values of this ratio are most often higher than in the measurements, except at OHP. The average ratio at all sites and seasons is slightly higher in the model (1.126) than in the data (1.043), although the average absolute deviation between model and data is large (20%), presumably mostly because of representativity issues. The coarse resolution of the model makes it impossible to reproduce the very large differences seen, for example, between the observed diurnal profiles at Beijing and Xianghe, two very nearby sites lying in the same model grid cell. OHP similarly lies in a region with strong gradients in the diurnal behavior of the columns, as seen in Fig. 3.

Nevertheless, the diurnal cycle of HCHO columns at the four most polluted sites (Uccle, Cabauw, Beijing and Xianghe) shows a consistent pattern during summertime (also in spring and fall at Uccle) which is well reproduced by the model. At Reunion Island as well, the observed midday maximum is well reproduced by the model. As pointed out above, the midday maximum at both very remote and very polluted sites is primarily caused by the diurnal cycle of OH levels, as the reaction with OH of the (mostly fairly long-lived) anthropogenic VOCs as well as methane is the main source of HCHO in those areas. In the Beijing area, the diurnal cycle of emissions is responsible for a slight delay in the maximum towards the afternoon, in agreement with the observations.

A broader network of measurements would be necessary to provide a more detailed assessment of HCHO column diurnal variations, in particular over forests and in biomass burning areas. Nevertheless, the comparison presented above with the limited dataset of available measurements revealed no large systematic discrepancies, except for a slight overestimation (by 8%) of the average ratio of 13h30 to 9h30 columns.

4 Satellite observations

The current version (v14) of the HCHO retrievals applied to GOME-2/METOP-A and OMI/AURA measurements is based on the algorithm developed for GOME-2 (version 12, De Smedt et al. (2012)), but with significant adaptations, as detailed below.

A classical DOAS algorithm is used, including three main steps: (1) the fit of absorption cross-section databases to the measured Earth reflectance in order to retrieve HCHO slant columns, (2) a background normalization procedure to eliminate remaining unphysical dependencies, and (3) the calculation of tropospheric air mass factors using radiative transfer calculations and modelled a priori profiles. In GOME-2 v12, two fitting intervals were introduced to improve the treatment of BrO absorption features, and to reduce the noise on the HCHO columns (328.5-359 nm for the pre-fit of BrO, 328.5-346 nm for the fit of HCHO) (De Smedt et al., 2012).

In the current version, a third fitting interval (339-364 nm) is used to pre-fit the O_2-O_2 slant columns in order to minimize the effect of spectral interferences between the molecular absorptions. This results in a global reduction of the HCHO slant columns over the continents compared to the previous version, by 0 to 25%, depending on the season and the altitude. It is interesting to note that the effect is very similar when applied to GOME-2 and OMI HCHO retrievals, i.e. it has little or no impact on the diurnal variations (De Smedt et al., 2015). In order to improve the fit of the slant columns, an iterative DOAS algorithm for removal of spike residuals has been implemented (Richter et al., 2011). In addition, this version of the algorithm makes use of radiance spectra, daily averaged in the equatorial Pacific, which serve as reference spectra. The background normalisation now depends on the day, the latitude, but also on the viewing zenith angle of the observation. This also serves as destriping procedure, needed for an imager instrument such as OMI (Boersma et al., 2011). The air mass factor calculation is based on Palmer et al. (2001). Scattering weighting functions are calculated with the LIDORT v3.3 radiative transfer model (Spurr, 2008).

The a priori profile shapes are provided by the IMAGES model, at 9h30 LT for GOME-2 and 13h30 LT for OMI (cf. Sect. 2). The OMI-based surface reflection database from Kleipool et al. (2008) is used for both GOME-2 and OMI. Radiative cloud effects are corrected using the independent pixel approximation (Martin et al., 2002) and the respective cloud products of the instruments provided by the TEMIS website (http://www.temis.nl), namely the GOME-2 O_2 A-band Frescov6 product (Wang et al., 2008) and the OMI O_2-O_2 cloud product (Stammes et al., 2008). As for the previous algorithm versions, v14 HCHO columns are openly available on the TEMIS website (http://h2co.aeronomie.be/).

Monthly averaged HCHO columns from both instruments gridded onto the resolution of the model are used as top-down constraints. The simulated monthly averaged columns are calculated from daily values weighted by the number of satellite (OMI or GOME-2) measurements for each day at each model grid cell. Columns with a cloud fraction higher than 40% are excluded from the averages. HCHO data are also excluded over oceanic IMAGES gridcells (for which the land fraction is lower than 0.2), since we aim to constrain only continental sources, as well as in the region of the South Atlantic geomagnetic anomaly, i. e. within less than 1500 km of its assumed epicentre (47.0 W, 24.9 S). Finally, regridded columns for which the monthly and spatially averaged retrieval error exceeds 100% are also rejected. The error of the satellite columns is defined as the square root of the squared sum of the retrieval error and an absolute error of $2{\cdot}10^{15}$ molec.cm^{-2}. In most VOC-emitting regions the error ranges between 40% and 60%.

The monthly regridded HCHO columns from GOME-2 and OMI are shown in Fig. 6 for July 2010. As seen in this figure, and discussed in De Smedt et al. (2015), the early afternoon columns of OMI are higher than the mid-morning values of GOME-2 at mid-latitudes, while the reverse is true at most tropical locations, in qualitative agreement with the ground-based measurements and modelling results (Figs. 4 and 5).

5 Inversion methodology

The flux inversion technique consists in minimizing the mismatch between the model predictions and a set of cemical observations by adjusting the a priori emission distributions $\Phi_i(x,t)$, where (x,t) denote the spatial (latitude, longitude) and temporal (year, month, day) variables, and i the different emission categories (biogenic, pyrogenic, anthropogenic). We express the optimized solution $\Phi_i^{opt}(x,t)$ as

$$\Phi_i^{opt}(x,t) = \sum_{j=1}^{m} e^{f_j}\Phi_i(x,t)$$

where $\mathbf{f} = (f_j)$ is the vector of variables to be determined so as to minimize the scalar function J (also termed as cost function)

$$J(\mathbf{f}) = \frac{1}{2}\left((H(\mathbf{f})-\mathbf{y})^T\mathbf{E}^{-1}(H(\mathbf{f})-\mathbf{y}) + \mathbf{f}^T\mathbf{B}^{-1}\mathbf{f}\right)$$

which measures the discrepancy between the modelled HCHO columns $H(\mathbf{f})$ and the observations $\mathbf{y}$. In this expression ^{T} is the transpose of the matrix, $\mathbf{E}$ and $\mathbf{B}$ are the matrices of errors on the observations $\mathbf{y}$ and on the variables $\mathbf{f}$, respectively. The gradient of the cost function J with respect to the input variables ($\partial J/\partial\mathbf{f}$) is calculated using the adjoint of the model. A thorough description of the method and its implementation in the IMAGESv2 CTM is given in Müller and Stavrakou (2005); Stavrakou et al. (2009b). The inversion is performed at the model resolution (2°x2.5°) using an iterative algorithm suitable for large scale problems (Gilbert and Lemaréchal, 1989).

The source inversions presented in Table 2 infer the emission rates of the three emission categories (anthropogenic, biogenic and biomass burning) are adjusted per month and are constrained by either GOME-2 or OMI HCHO columns. On the global scale, ca. 63,000 flux parameters are varied. The emission of a grid cell is not optimized when its maximum a priori monthly value is lower than 10^{10} molec.cm^{-2} s^{-1}. The assumed error on the a priori anthropogenic emission by country is set equal to a factor 1.5 and 2 for OECD and other countries, respectively, to a factor of 2 for biogenic emissions and 3 for fire burning emissions (Stavrakou et al., 2009b).

The sensitivity studies (Table 2) aim at assessing the impact of (i) the choice of a priori errors on the emission fluxes (OMI-DE, OMI-HE), (ii) the cloud fraction filter applied to the satellite data (OMI-CF), and (iii) the isomerization of isoprene peroxy radicals (OMI-IS). The annual a priori and top-down fluxes of the two standard and the four sensitivity inversions are summarized in Table 3. The a priori model columns calculated at 9h30 and 13h30 local time are generally higher than the GOME-2 or OMI HCHO column abundances (Fig. 6), e. g. over Europe, Southern China, the United States, Amazonia and Northern Africa. They are however found to agree generally well in terms of seasonality (Fig. 7).

6 Overview of the results

Globally, the cost function is reduced by a factor of 2 after optimization, and its gradient is reduced by a factor of ca. 10^3. In general, the consistency between the two inversions is highest in tropical regions. At mid-latitudes, the emission updates (i.e. the ratios of optimized to prior emissions) are almost systematically higher in the OMI-based than in the GOME-2-based inversion. This reflects ratios of 13h30 to 9h30 columns which are lower in the model than suggested by the two satellite datasets.

Both GOME-2 and OMI inversions suggest a strong decrease in global biomass burning VOC emissions with regard to the a priori GFEDv3 inventory, by 36% and 33%, respectively. This decrease is most pronounced in tropical regions. In contrast, both the OMI and GOME-2 optimizations lead to enhanced emissions (by about 50%) due to the extensive fires which plagued European Russia in August 2010 (Sect. 7.2) and to agricultural waste burning in the North China Plain in June (Sect. 7.3). The fire burning estimates from the two base inversions are generally quite consistent, not only globally but also over large emitting regions like Amazonia, Southeastern Asia, and Africa. The sensitivity studies provide global flux estimates which are close (within 7%) to the standard top-down results using OMI.

The globally derived isoprene fluxes are reduced in both standard inversions, by 9% according to GOME-2 and by 13% according to OMI, compared to the a priori estimate of the MEGAN-ECMWF-v2 inventory (363.1 Tg/yr, Table 3). The overall consistency between the global estimates is high for this emission category, despite some significant differences at a regional scale (cf. next sections). The biogenic top-down fluxes derived from the sensitivity inversions of Table 2 lie within 5% of the OMI-based estimates on the global scale, yet larger differences are found in the regional scale.

Finally, the global anthropogenic source is decreased in the GOME-2 inversion, while it is slightly increased in the inversion using OMI. Despite their limited capability to constrain this emission category on the global scale due to its small contribution to the global HCHO budget (Stavrakou et al., 2009a), the satellite observations are found to provide constraints over highly polluted regions, notably Eastern China, where however the discrepancy between the two sensors is most evident (see Sect. 7.3).

Annual emission updates for the different source categories, and the monthly variation of the a priori and optimized flux estimates are illustrated in Figs. 9, 10, 11, 12 and 13.

Modifying the errors on the flux parameters infers global isoprene emission decreases of ca. 15% (OMI-HE) and 30% (OMI-DE) with regard to the initial isoprene inventory, and within 7% of the standard OMI inversion, cf. Table 3. As expected, due to the limited or stronger confidence assigned to the a priori inventories in OMI-DE and OMI-HE scenarios, respectively, most substantial departures from the a priori inventory are obtained when doubling the errors on the emission parameters, while the OMI-HE scenario lies closer to the a priori database. The impact of the use of a stricter cloud criterion on the OMI scenes used as top-down constraints (20% for OMI-CF instead of 40% in OMI base inversion) results in weak increases of the globally inferred fluxes with respect to the OMI inversion, but the enhancement is more important in extratropical regions, and amounts to 22% for biomass burning emissions (Table 3 and left panel of Fig. 8). Finally, suppressing the isomerization channel in isoprene oxidation increases the HCHO yield from isoprene and leads to slightly higher model columns over isoprene-rich regions. As seen on the right panel of Fig. 8, the resulting isoprene fluxes are only slightly lower compared to the reference run (by 4% lower on the global scale). Over Amazonia, this emission reduction reaches 8%.

7 Emissions at the mid-latitudes

7.1 North America

Biogenic isoprene emissions drive the HCHO column seasonality and explain the summertime column peak in the Eastern US (Fig. 7). The a priori model exhibits, however, a much stronger seasonal variability than the observation with a summer-to-winter ratio of 4-5 compared to the observed ratio of about 2. In summertime, the a priori model overestimates the GOME-2 and OMI measurements by up to 50% and 35%, respectively in the Eastern US. This drives the significant decrease in the optimized isoprene fluxes, from the a priori value of 17.8 Tg to 11.6 Tg (GOME-2) and to 13.8 Tg (OMI) over the US in 2010, in good agreement with our earlier flux estimates (13 Tg/yr) based on SCIAMACHY HCHO columns (Stavrakou et al., 2009b). Even larger reductions are found in the Southeastern US, amounting to ca. 25% and 40% in the OMI and GOME-2 inversions, respectively

(Fig. 13). Anthropogenic and pyrogenic emissions over the US are essentially unchanged by the inversions.

The estimated cumulative June-August US isoprene emissions from both optimizations (7.8 Tg for GOME-2 and 9.5 Tg for OMI) agree well with reported values based on earlier versions of OMI HCHO retrievals (9.3 Tg according to the variable slope technique as described in Millet et al. (2008)). The OMI-based isoprene flux in July 2010, estimated at 3.23 Tg, is by 30% lower than the a priori (4.62 Tg), corroborating the low values of the BEIS2 inventory (Palmer et al., 2003).

The model predictions are compared to HCHO measurements from the INTEX-A aircraft campaign conducted in July-August 2004 over the Eastern US (Singh et al., 2006; Fried et al., 2008) in Fig. 14. It is worth noting that the measurements by NCAR (National Center for Atmospheric Research) and URI (Univ. Rhode Island) exhibit large differences between them, the NCAR values being by ca. 50% higher than URI below 2 km altitude (Fig. 14). The model simulations are performed for 2004, and the concentrations are sampled at the locations and times of the airborne measurements. In the a posteriori simulation shown in Fig. 14, the bottom-up isoprene emissions for 2004 were multiplied by the isoprene emission update inferred from either the OMI or the GOME-2 inversion for 2010. As seen in Fig. 14, the average HCHO concentration below 2 km altitude is decreased by about 10% in the OMI inversion (15% in the case of GOME-2) and remains within the range of the NCAR and URI measurements. Despite the marked underestimation of the modelled HCHO (1.39 and 1.32 ppbv in the OMI and GOME-2 inversions) in comparison to NCAR observations (1.83 ppbv), the emission optimization results in an increased Pearson's spatial correlation coeffient between the modelled and observed concentrations below 2 km, from 0.74 in the a priori to 0.79 and 0.80 in the OMI and GOME-2 inversions. A similar improvement is found with respect to URI data.

7.2 Russia

The a priori model underpredicts the observed OMI HCHO columns during the Russian fires of July-August 2010 by up to a factor of 2, in particular over a broad region extending to the North (61 N) and East (55 E) of Moscow (Fig. 6, upper panel). Similar spatial patterns are also observed in GOME-2 HCHO columns. However, the GOME-2 columns are lower than OMI over this region, and the model underestimation is less severe in this case reaching 60%. The lower GOME-2 values might be due to the lower retrieval sensitivity of GOME-2 to lower tropospheric HCHO compared to OMI at these latitudes, associated to larger solar zenith angles (De Smedt et al., 2015). As a result, the increase of the pyrogenic emission fluxes is strongest in the OMI inversion, from 440 Gg VOC in the GFEDv3 inventory, to 720 Gg VOC (630 GgVOC in GOME-2) in August 2010 over Europe. Accordingly, the isoprene fluxes inferred from the OMI inversion in August are also larger, about 40% higher than the a priori estimate in the Moscow area, whereas the increase derived by GOME-2 does not exceed 25%. Overall, the OMI data suggest annual isoprene fluxes in Europe by 11% higher than the a priori inventory (Table 3). Note that, although the isoprene enhancement over Russia peaks earlier (July) and at slightly higher latitudes (ca. 61° N) than the biomass burning emission enhancement (55–57° N in August), the significant overlap of the two distributions makes impossible to rule out that pyrogenic emissions are the only cause for the observed strong formaldehyde columns. The very widespread extent of the observed formaldehyde plume cannot be easily explained by the comparatively much more localized emissions of the GFED3 inventory, and an additional, more widespread formaldehyde source (such as isoprene) could help to explain the observations. However, as discussed below, the GFED3 total emissions over Russia are likely largely underestimated, and their geographical distribution might also be in error. It is therefore possible that these fires were more widespread than in GFED3 and that strong isoprene emission enhancements are not needed to explain the observations.

Strongly enhanced fire emissions in the Moscow region between mid-July and mid-August 2010 were reported based on satellite observations of CO from MOPITT (Konovalov et al., 2011) and IASI (Krol et al., 2013; R'honi et al., 2013), and on suface measurements (Konovalov et al., 2011). The optimized fire emission inferred by assimilation of IASI CO columns in Krol et al. (2013) lies within 22 and 27 Tg CO during the fires, i.e. about 7-10 times higher than in the bottom-up inventory (GFEDv3). These values are comparable with the ranges of 19-33 and 34-40 Tg CO suggested by R'honi et al. (2013) and Yurganov et al. (2011), respectively, but are much higher than reported values of ca. 10 Tg CO derived using surface CO measurements in the Moscow area (Konovalov et al., 2011). The latter study identifies the contribution of peat burning to the total CO fire emission in this region to be as high as 30%.

The IMAGESv2 a priori CO simulation (using GFEDv3 inventory) underestimates substantially the IASI CO observations. Scaling the CO emissions in IMAGESv2 to the fire VOC increase suggested by the OMI HCHO optimization, i.e. ca. 60% in July and August 2010, barely improves the model agreement with the satellite, indicating that, in accordance with earlier studies, more drastic fire flux enhancements (factor of 5 to 10) are required to reconcile CO model-data mismatches. The reasons for the differences in the emission increases inferred by CO and HCHO during the 2010 Russian fires are currently unknown, but could be related either to inadequate knowledge of emission factors of CO and VOCs from peat fires, and/or underestimated remote-sensed HCHO columns over fire scenes due to possibly important aerosol effects not accounted for in the retrievals.

7.3 China

The dominant emission source in China is anthropogenic and is estimated at 25.5 TgVOC in REASv2 (Kurokawa et al., 2013) for 2008. The biogenic source, mainly located in Southern China, amounts to 7 Tg in 2010 in the MEGAN-MOHYCAN-v2 inventory (Stavrakou et al., 2014; Guenther et al., 2006, 2012). In Northern China, the HCHO columns are underestimated by the a priori model in winter compared to OMI, whereas a relatively good agreement is found in summer. In Southern China, a general model overestimation is found all year round (Figs. 6 and 7).

Although the OMI-based inversion yields total Chinese anthropogenic emissions very similar to the a priori (24.6 TgVOC), the emission patterns are modified with increased emissions in Northeast China and especially around Beijing (20-40%), and emission reductions in the Southeast and in particular around Shanghai (15-47%) and Guangzhou (15-30%). The total GOME-2 emission, estimated at 20.6 TgVOC, is lower than the OMI result, but in good agreement with the estimate (20.2 Tg in 2008) of the Multi-resolution Emission Inventory for China (MEIC, http://www.meicmodel.org). The flux distributions from both inversions have common features, e.g. decreased fluxes in Shanghai and Guangzhou regions, but contradicting estimates in the Northeast where GOME-2 observations do not support the emission enhancements suggested by OMI.

This discrepancy is primarily due to the lower modelled ratios of 13h30 to 9h30 columns (average ratio of 1.0 in the model in North China between March and November) compared to the satellite datasets (average ratio of 1.16). Note that, however, the model was found to overestimate this ratio against MAX-DOAS data at Beijing and Xianghe (Fig. 5). Another possible cause for difference between the OMI and GOME-2 results is the limited availability of GOME-2 data in wintertime (Fig. 7) due to the high solar zenith angles leading to large retrieval errors frequently exceeding 100%. For example, GOME-2 columns are unavailable from November to April over Beijing.

In the North China Plain, one of the largest agricultural plains on Earth, the post wheat harvest season fires set up every year in June is a common farmer's practice (Huang et al., 2012), responsible for poor air quality conditions and environmental harm (Yamaji et al., 2010). Both OMI and GOME-2-based inversions suggest a considerable enhancement of the agricultural fire flux in this region, by almost a factor of 2 in comparison with the a priori inventory by Huang et al. (2012), cf. Fig. 12. The interannual variability of these emissions will be addressed in a separate work in preparation.

Finally, the Chinese isoprene emission are decreased from 7 Tg per year to 6.5 Tg (OMI) and 5.9 Tg (GOME-2), with especially strong decreases in Southern China, as illustrated in Fig. 10.

8 Emissions in the Tropics

8.1 South America

After the 2005 drought in Amazonia, characterized as one-in-a-century event (Marengo et al., 2008), Amazonia suffered a second, even more severe drought in 2010 with major environmental impacts (Marengo et al., 2011). Extensive wildfires broke out in different regions from July to October, with central and south Amazonia as main epicenters. The massive fire burning is reflected in the high HCHO columns (up to $15{\cdot}10^{15}$ molec.cm^{-2}) detected by GOME-2 and OMI during these months, about twice the observed columns in the wet season (Fig. 7). Both instruments agree very well on the magnitudes and spatial patterns of the HCHO columns, as illustrated in Fig. 15. The a priori model strongly overestimates the observations during the dry season (by up to 70% in August) indicating that the GFEDv3 emissions for this region are most likely too high. The GOME-2 and OMI inversions decrease the fire emission by factors of 2 and 2.5, respectively (Fig. 12). Even stronger decreases (factor of 3) are found over Northern Bolivia and central Amazonia (Fig. 9).

These emission reductions are supported by comparison with CO columns observed by IASI (George et al., 2009). The use of fire emissions from GFEDv3 leads to strongly overestimated CO columns in comparison to IASI observations in August 2010 (Fig. 15), reaching almost a factor of 2 over Western Amazonia. Significant improvement in the model-data match is achieved when the emission reduction inferred by the OMI-based inversion is implemented and applied not only to NMVOCs but also to other compounds including CO. The GFEDv3 emissions of CO in 2010 were also found to be substantially overestimated, by a factor of $\sim$1.8 over South America between 5°S and 25°S, by inverse modelling of MOPITT CO columns using the GEOS-Chem model (Bloom et al., 2015). The most likely cause for the lower emissions in 2010 compared to 2007 was proposed by these authors to be a reduction of the combusted biomass density possibly due to dry conditions and/or repeat fires. The good consistency found between results using either CO or HCHO indicates that the emission factors used in the model for NMVOC and CO (or at least their ratios) are appropriate, unless an error compensation is responsible for the noted good agreement. Note also that, besides the good consistency found between the emission estimates derived from GOME-2 and OMI, the performed sensitivity inversions induce only very weak departures from the standard inversion (Fig. 12).

Isoprene fluxes over Amazonia derived by GOME-2 and OMI inversions are equal to 92.5 Tg and 73.7 Tg, respectively. This is by 25% and 7% lower than the prior and in good agreement with previous studies using satellite HCHO observations from the SCIAMACHY instrument (Stavrakou et al., 2009b). The seasonal variation of the posterior fluxes is consistent with the a priori inventory, except during the transitional wet-to-dry period (April-June) with both GOME-2 and OMI satellite datasets pointing to a significant flux decrease by ca. 25% (Fig. 13). This behaviour confirms previous comparisons using GOME HCHO observations suggesting that factors other than the temperature influence the observed variability (Barkley et al., 2008), such as the growth of new leaves causing a temporary shut-down of the emissions (Barkley et al., 2009).

8.2 Indonesia

Fire activity was exceptionally low in 2010, with annual emissions of about 0.1 TgVOC, i. e. about two orders magnitude less than for high years such as 2006 according to GFEDv3.

The GOME-2 and OMI inferred isoprene estimates show good consistency over Indonesia all year round, amounting to 10.3 Tg and 11.1 Tg, respectively, close to the a priori (11.6 Tg). The inferred isoprene emissions are, however, twice lower than reported fluxes of 25 Tg/yr based on SCIAMACHY HCHO observations, which were themselves decreased with respect to their priori isoprene flux of 35 Tg/yr (Stavrakou et al., 2009b). In comparison to that study, the isoprene a priori emissions used in the present work are strongly reduced over this region, due to a drastic reduction by a factor of 4.1 of the MEGANv2.1 basal isoprene rate for tropical rainforests over Asia, as suggested by field measurements in Borneo (Langford et al., 2010). This reduction implemented in the MEGAN-MOHYCAN-v2 model (Stavrakou et al., 2014) is found here to be corroborated by GOME-2 and OMI HCHO measurements.

8.3 Indochina

The Northern part of the Indochinese peninsula (primarily Myanmar, also Assam in India and parts of Thailand) faces intense forest fires during the dry season, as very well seen in the GOME-2 and OMI HCHO timeseries, with values reaching $15{\cdot}10^{15}$ molec.cm^{-2} in March, about three times higher than in the wet season (Fig. 7).

Both the GOME-2 and OMI data point to substantial, but very contrasting updates in the pyrogenic fluxes during the fire season (March, Fig. 9): flux reductions by a factor of 2–5 over Myanmar and surrounding forested areas, and flux increases by a factor of almost 2 (or more in the case of OMI) over the Southeastern part of the peninsula, which includes Cambodia, Southern Laos and Southern Vietnam. In the OMI-DE inversion assuming doubled errors on the a priori fluxes, the updates are even more pronounced and reach a factor of 4 over parts of Vietnam and Laos. The annual emissions in the entire region are decreased by 15% and 26% according to the OMI and GOME-2 inversions, respectively. As illustrated in Fig. 16, the optimization leads to a substantial improvement of the model performance, although the HCHO columns remain significantly underestimated (by up to 20%) in the Southern part of the peninsula (e. g. Cambodia), most likely due to a too strong underestimation of the GFEDv3 emissions used as a priori in the model. The emission drop over Myanmar and the need for higher emissions in the Southeast are partly confirmed by comparisons with IASI CO columns. Indeed, as seen on the lower panel of Fig. 16, modelled CO simulations using biomass burning fluxes optimized using OMI data (i.e. reduced by ca. 26% in March relative to GFED3) display a better agreement with the observed CO columns, despite an underestimation by $\sim$10% over most of the peninsula. This result is consistent with the moderate reduction (ca. 20% in March) of biomass burning emissions of CO over Tropical Asia inferred by Basu et al. (2014) in an inversion based on IASI CO columns utilizing the TM5 atmospheric model with GFED3 as a priori inventory.

The strong enhancement of pyrogenic emissions required to comply to the satellite data over the Southeastern part of Indochina might be due to the occurrence of agricultural fires in those regions (e. g. Cambodia), known to be a common management practice (Chang and Song, 2010). These fires are very difficult to detect by satellite due to their limited spatial extent. It is worth noting that the latest version of the Fire Inventory from NCAR (Wiedinmyer et al., 2011) (FINNv1.5) predicts much higher emissions from this region : ca. 43 TgC in March in the region 100–108 E, 10–18 N, i.e. a factor of 10 higher than in the GFEDv3 inventory (4.3 TgC). The differences between GFEDv3 and FINN are most likely due to inherent differences in the proxy variables used in the respective emission models, burned area in the case of GFEDv3, and active fire counts in FINN model, both retrieved from MODIS satellite data. The two inventories provide however very similar estimates for the more forested, Northwestern part of Indochina (19–27 N, 97–100 E): 105 TgC in GFEDv3, 124 TgC in FINNv1.5.

Considerable cloudiness during the rainy season (May-October) causes gaps in the OMI HCHO timeseries, due to the exclusion of scenes with $\geq$40% cloud cover. The GOME-2 data series are comparatively less affected by this issue, due to the diurnal precipitation and cloudiness patterns during the monsoon season. Indeed, long-term observations over Indochina (Takahashi et al., 2010) reveal an early afternoon rainfall peak (13-16h LT), and heavy rainfall in the early morning (4-7h), but lower precipitation rates between 7 and 10h. GOME-2 observations are therefore less contaminated by clouds and offer a better spatial coverage during the rainy season in this region.

8.4 Africa

Over Africa, the annual pyrogenic source, amounting at 40.7 TgVOC in the a priori, is reduced to 26.2 and 32.6 TgVOC in the GOME-2 and OMI inversions, respectively (Table 3). A smaller reduction is also inferred for isoprene fluxes, estimated at 76.6 Tg (GOME-2) and at 74.2 Tg (OMI), within 10% of the a priori value (81.6 Tg). These estimates are in line with recently reported isoprene fluxes over Africa based on the NASA dataset of OMI HCHO columns (77 Tg C or 87 Tg isoprene compared to 116 Tg isoprene in the a priori, Marais et al. (2012)). The spatial distribution of the emission updates is displayed in Figs. 9, 10 and 11.

African fire occurrence peaks in central Africa (e. g., the Democratic Republic of the Congo or DRC) in early June (Fig. 7) and lasts until August with the end of the dry season. The GOME-2 and OMI observations show an excellent accordance, with morning columns being about 10% higher than in the afternoon, consistent with measurements in Bujumbura (Fig. 5), although the morning-to-afternoon ratio was found to be higher in the ground-based observations (1.25). The model simulations overpredict the observations of both sounders during the fire season by 10-25%. The posterior bias reduction (cf. Fig. 7, DRC region) is achieved by a significant biomass burning flux decrease, reaching a factor of 2 in the southern part of DRC, and 20-30% elsewhere between 2 and 12°S. In a similar manner, up to a factor of 2 emission decrease is also needed in the region of the Central African Republic during the fire season (November-February) to match the observed columns (Fig. 7), in good agreement with our previous study using SCIAMACHY HCHO columns (Stavrakou et al., 2009b). Only small changes are inferred for isoprene emissions in Northern Africa, by 11% (GOME-2) and by 16% (OMI) decrease compared to the a priori, as illustrated in Fig. 13.

In Southern Africa, biogenic fluxes are highest in January and lowest in July, while the fire season starts in May, and peaks in September (Figs. 12 and 13). Both GOME-2 and OMI inversions infer only small isoprene flux updates (Table 3). Regarding fire emissions, in constrast with GOME-2 data suggesting a ca. 30% flux reduction (to 17.6 from 25.8 TgVOC), the OMI-based estimate lies within 10% of the a priori, due to a compensation of flux decreases North of approx. 15 S, and flux increases in the southernmost part of the continent, south of ca. 15 S (Fig. 9). Although the seasonal patterns are essentialy preserved by the optimization, both inversions predict higher emissions at the end of the dry season, especially over Zambia and surrounding regions (October, Fig. 12). These updates are highest (factor of $\sim$2) in the OMI optimization, but the patterns are very similar in both inversions.

9 Conclusions

The emissions of NMVOCs in 2010 were optimized by inverse modelling using the IMAGESv2 CTM and its adjoint with HCHO column abundances from either GOME-2 or OMI as observational constraint. Given their different overpass times, the consistency of the inferred emissions depends on how the model can faithfully reproduce the diurnal cycle of HCHO columns. The modelled diurnal cycle displays a great variability mirroring the competing influences of photochemical productions and losses as well as the diurnal profiles of emissions and (to a lesser extent) meteorological parameters. Where anthropogenic VOCs are dominant, daytime photochemical production and the anthropogenic emission profile leads to an early afternoon maximum, in agreement with MAX-DOAS observations in Belgium, Holland and (during summertime) the Beijing area. Over oceanic areas, where methane oxidation is the only significant source in the model, a similar behavior is also simulated, in agreement with FTIR data at Reunion Island. The poor model performance at several locations (Bujumbura, OHP, Beijing in winter/spring) is likely at least partly due to the coarse model resolution, as shown by the very different diurnal profiles observed at Beijing and Xianghe. This limited representativity of local ground-based sites possibly explains (part of) the large deviations (typically $\pm$10-30%) found between the calculated and observed ratios of the HCHO columns at 13h30 and 9h30. Despite this large scatter, the average ratio of 13h30 columns to 9h30 columns is only slightly higher (1.126) in the model compared to the MAX-DOAS and FTIR measurements (1.043).

Unfortunately no ground-based measurements are available in regions where the simulated diurnal cycle amplitude is largest, namely over intense fire scenes at both tropical and boreal latitudes. Over these regions, an evening maximum is predicted, and the peak-to-trough ratio reaches up to 70%. In isoprene-rich areas, the diurnal HCHO cycle often, but not always, displays a minimum around noon, when the photochemical sink is highest, and a maximum in the late evening or early morning, in agreement with a previous modelling study (Barkley et al., 2011). Validation studies over forested areas will be needed to determine how realistic these patterns are.

The ratio of 13h30 to 9h30 column is most often between 0.8 and 1.2 according to ground-based measurements. Similar, but generally higher values of this ratio are calculated by the model, by 8% on average. The satellite, on the other hand, although in qualitative agreement with the above, suggests higher ratios of 13h30 to 9h30 columns than the model at mid-latitudes, whereas no clear pattern emerges in tropical regions (Fig. 7). Nevertheless, these discrepancies in terms of morning/afternoon ratios are most often small in comparison with the model/data differences in the HCHO columns themselves. As a consequence, the emission fluxes inferred from both GOME-2 and OMI inversions are found to be generally very consistent. They both suggest a strong decrease of the global biomass burning source, by about 35%. The decrease is mostly concentrated in the Tropics, e.g. over Amazonia (factor of >2 reduction), over Equatorial Africa and over Myanmar and surrounding regions (factor of 2–5 reduction in March). These updates are confirmed by comparing CO columns predicted by the model using the biomass burning emissions estimated by the OMI inversion with IASI CO columns. The results are also consistent with a recent study using MOPITT CO columns (Bloom et al., 2015). The seasonal profile of the emissions is generally well preserved by the inversions, except for a significant enhancement near the end of the dry season, in particular over Southern Africa (in October) but also Amazonia (in September) and Indochina (in April). Both satellite datasets point to strong enhancements of agricultural fire fluxes in the North China Plain in June (factor of almost 2) and in the southern part of Indochina, compared to the a priori estimate.

Very good agreement between the inversion results is found for isoprene fluxes, with global annual fluxes reduced by 9% (GOME-2) and 13% (OMI) compared to the a priori of 363 Tg. In the Southeastern US, both inversions agree on a substantial decrease by ca. 25% (OMI) and 40% (GOME-2), in good agreement with previous estimates based on SCIAMACHY and OMI HCHO data. This reduction improves the correlation between calculated and observed HCHO concentrations during the airborne INTEX-A campaign conducted over the Eastern US. Over Amazonia, the source of isoprene is consistently lower than the a priori, in particular during the wet-to-dry season transition (April–June), in accordance with previously reported estimates. Over Indonesia, the optimizations do not present significant deviations from the prior, thereby validating the a priori isoprene inventory which incorporated decreased basal emission rates for Asian tropical rainforests.

The results show that the global anthropogenic VOC fluxes are not well constrained, as indicated by the negligible updates derived by the inversions over most areas, except over highly polluted regions with a distinct anthropogenic signal in the HCHO columns, like China. In this region, the changes in the emission patterns found by the OMI-based optimization are not well reproduced by the inversion of GOME-2 data, likely reflecting discrepancies in the 13h30/9h30 column ratio calculated by the model. In spite of those discrepancies, our study demonstrates that a high degree of compatibility is achieved between top-down pyrogenic and biogenic emissions derived by GOME-2 and OMI HCHO data, while the flux estimates are found to be weakly dependent to changes in key uncertain parameters in the performed sensitivity inversions.

This study identifies several important large regions where the differences between bottom-up and top-down estimates are particularly important and the inferred flux estimates from both satellites show a high degree of consistency, like the Amazon and the Southeast US. Recent airborne field measurements in those regions should provide additional constraints and help close the gap between bottom-up and top-down estimates. The increasing availability of in-situ observations of formaldehyde and related trace gases can provide a basis for improving and assessing model simulations of diurnal variations over a range of environmental conditions and interactions between biogenic and anthropogenic compounds (e.g. DiGangi et al. (2012)). Furthermore, planned geostationary satellites have the potential to improve satellite based emission estimates by characterizing diurnal variations in atmospheric constituents (Saide et al., 2014). Finally, new cross section measurements of isoprene in the infrared open new avenues for the detection of isoprene using satellite (e.g. IASI) and a direct link to isoprene emission (Brauer et al., 2014).

Acknowledgements. This research was supported by the Belgian Science Policy Office through the PRODEX projects ACROSAT and IASI.Flow (2014-2015), and by the European Space Agency (ESA) through the GlobEmission project (2011-2016). P.-F.C. is senior research associate with FRS-FNRS.

References

Andreae, M.O., and P. Merlet : Emission of trace gases and aerosols from biomass burning, Global Biogeochem. Cy., 15(4), 955–966, doi:10.1029/2000GB001382, 2001.

Arneth, A., G. Schurgers, J. Lathière, T. Duhl, D. J. Beerling, C. N. Hewitt, M. Martin, and A. Guenther : Global terrestrial isoprene emission models: sensitivity to variability in climate and vegetation, Atmos. Chem. Phys., 11, 8037–8052, doi:10.5194/acp-11-8037-2011, 2011.

Barkley, M. P., P. I. Palmer, U. Kuhn, J. Kesselmeier, K. Chance, T. P. Kurosu, R.V. Martin, D. Helmig, and A. Guenther : Net ecosystem fluxes of isoprene over tropical South America inferred from Global Ozone Monitoring Experiment (GOME) observations of HCHO columns, J. Geophys. Res., 113, D20304, doi:10.1029/2008JD009863, 2008.

Barkley, M. P., P. I. Palmer, I. De Smedt, T. Karl, A. Guenther, and M. Van Roozendael : Regulated large-scale annual shutdown of Amazonian isoprene emissions? Geophys. Res. Lett., 36, L04803, doi:10.1029/2008GL036843, 2009.

Barkley, M. P., P. I. Palmer, L. Ganzeveld, A. Arneth, D. Hagberg, T. Karl, A. Guenther, F. Paulot, P. O. Wennberg, J. Mao, T. P. Kurosu, K. Chance, J.-F. Müller, I. De Smedt, M. Van Roozendael, D. Chen, Y. Wang, and R. M. Yantosca : Can a “state of the art” chemistry transport model simulate Amazonian tropospheric chemistry? J. Geophys. Res., 116, D16302, doi:10.1029/2011JD01589, 2011.

Barkley, M. P., I. De Smedt, M. Van Roozendael, T. P. Kurosu, K. Chance, A. Arneth, D. Hagberg, A. Guenther, F. Paulot, E. Marais, and J. Mao : Top-down isoprene emissions over tropical South America inferred from SCIAMACHY and OMI formaldehyde columns, J. Geophys. Res. Atmos., 118, 6849–6868, doi:10.1002/jgrd.50552, 2013.

Basu, S., M. Krol, A. Butz, C. Clerbaux, Y. Sawa, T. Machida, H. Matsueda, C. Frankenberg, O. P. Hasekamp, and I. Aben : The seasonal variation of the CO_2 flux over Tropical Asia estimated from GOSAT, CONTRAIL, and IASI, Geophys. Res. Lett., 41, 1809–1815, 2014.

Bloom, A. A., J. Worden, Z. Jiang, H. Worden, T. Kurosu, C. Frankenberg, and D. Schimel : Remote sensing constraints on South America fire traits by Bayesian fusion of atmospheric and surface data, Geophys. Res. Lett., accepted for publication, doi: 10.1002/2014GL062584, 2015.

Bloss, C., V. Wagner, A. Bonzanini, M. E. Jenkin, K. Wirtz, M. Martin-Reviejo, and M. J. Pilling : Evaluation of detailed aromatic mechanisms (MCMv3 and MCMv3.1) against environmental chamber data, Atmos. Chem. Phys., 5, 623–639, 2005.

Boersma, K. F., H. J. Eskes, R. J. Dirksen, R. J. van der A, J. P. Veefkind, P. Stammes, V. Huijnen, Q. L. Kleipool, M. Sneep, J. Claas, J. Leitão, A. Richter, Y. Zhou, and D. Brunner : An improved tropospheric NO_2 column retrieval algorithm for the Ozone Monitoring Instrument, Atmos. Meas. Tech., 4, 1905-1928, 2011.

Brauer, C. S., T. A. Blake, A. B. Guenther, S. W. Sharpe, R. L. Sams, and T. J. Johnson : Quantitative infrared absorption cross sections of isoprene for atmospheric measurements, Atmos. Meas. Tech., 7, 3839-3847, 2014.

Chance, K., P. I. Palmer, R. J. D. Spurr, R. V. Martin, T. Kurosu, and D. J. Jacob : Satellite observations of formaldehyde over North America from GOME, Geophys. Res. Lett., 27, 3461–3464, 2000.

Chang, D., and Y. Song : Estimates of biomass burning emissions in tropical Asia based on satellite-derived data, Atmos. Chem. Phys., 10, 2335–2351, 2010.

Choi, W., I. C. Faloona, N. C. Bouvier-Brown, M. McKay, A. H. Goldstein, J. Mao, W. H. Brune, B. W. LaFranchi, R. C. Cohen, G. M. Wolfe, J. A. Thornton, D. M. Sonnenfroh, and D. B. Millet : Observations of elevated formaldehyde over a forest canopy suggest missing sources from rapid oxidation of arboreal hydrocarbons, Atmos. Chem. Phys., 10, 8761–8781, doi:10.5194/acp-10-8761-2010, 2010.

Crounse, J. D., F. Paulot, J. G. Kjaergaard, and P. O. Wennberg: Peroxy radical isomerization in the oxidation of isoprene, Phys. Chem. Chem. Phys., 13, 13607–13613, 2011.

Damian, V., A. Sandu, M. Damian, F. Potra, and G. R. Carmichael : The Kinetic PreProcessor KPP - A Software Environment for Solving Chemical Kinetics, Comput. Chem. Eng., 26, 1567–1579, 2002.

De Smedt, I., J.-F. Müller, T. Stavrakou, R. van der A, H. Eskes, M. Van Roozendael : Twelve years of global observations of formaldehyde in the troposphere using GOME and SCIAMACHY sensors, Atmos. Chem. Phys., 8, 4947–4963, 2008.

De Smedt, I., M. Van Roozendael, T. Stavrakou, J.-F. Müller, C. Lerot, N. Theys, P. Valks, N. Hao, and R. van der A : Improved retrieval of global tropospheric formaldehyde columns from GOME-2/MetOp-A addressing noise reduction and instrumental degradation issues, Atmos. Meas. Tech., 5, 2933–2949, 2012.

De Smedt, I., T. Stavrakou, F. Hendrick, T. Danckaert, T. Vlemmix, G. Pinardi, N. Theys, C. Lerot, J.-F. Müller, P. Veefkind, M. Van Roozendael : Diurnal, seasonal and long-term variations of global formaldehyde columns inferred from combined OMI and GOME-2 observations, submitted to Atmos. Chem. Phys., 2015.

DiGangi, J. P., S. B. Henry, A. Kammrath, E. S. Boyle, L. Kaser, R. Schnitzhofer, M. Graus, A. Turnipseed, J.-H. Park, R. J. Weber, R. S. Hornbrook, C. A. Cantrell, R. L. Maudlin, S. Kim, Y. Nakashima, G. M. Wolfe, Y. Kajii, E. C. Apel, A. H. Goldstein, A. Guenther, T. Karl, A. Hansel, and F. N. Keutsch : Observations of glyoxal and formaldehyde as metrics for the anthropogenic impact on rural photochemistry, Atmos. Chem. Phys., 12, 9529–9543, doi:10.5194/acp-12-9529-2012, 2012.

Dufour, G., F. Wittrock, M. Camredon, M. Beekmann, A. Richter, B. Aumont, and J. P. Burrows : SCIAMACHY formaldehyde observations: constraint for isoprene emission estimates over Europe? Atmos. Chem. Phys., 9, 1647–1664, doi:10.5194/acp-9-1647-2009, 2009.

Fried, A., J. G. Walega, J. R. Olson, J. H. Crawford, G. Chen, P. Weibring, D. Richter, C. Roller, F. Tittel, B. G. Heikes, J. A. Snow, H. Shen, D. W. O'Sullivan, M. J. Porter, H. E. Fuelberg, J. J. Halland, and D. B. Millet : Formaldehyde over North America and the North Atlantic during the summer 2004 INTEX campaign : Methods, observed distributions and measurement comparisons, J. Geophys. Res., 113, D10302, doi:10.1029/2007JD009185, 2008.

Fu, T.-M., D. J. Jacob, P. I. Palmer, K. Chance, Y. X. Wang, B. Barletta, D. R. Blake, J. C. Stanton, and M. J. Pilling : Space-based formaldehyde measurements as constraints on volatile organic compound emissions in east and south Asia and implications for ozone, J. Geophys. Res., 112, D06312, doi:10.1029/2006JD007853, 2007.

Fuchs, H., A. Hofzumahaus, F. Rohrer, B. Bohn, T. Brauers, H-P. Dorn, R. Häseler, F. Holland, M. Kaminski, X. Li, K. Lu, S. Nehr, R. Tillmann, R. Wegener, and A. Wahner : Experimental evidence for efficient hydroxyl radical regeneration in isoprene oxidation, Nature Geosci., 6, 1023–1026, doi:10.1038/ngeo1964, 2013.

George, M., C. Clerbaux, D. Hurtmans, S. Turquety, P.-F. Coheur, M. Pommier, J. Hadji-Lazaro, D. P. Edwards, H. Worden, M. Luo, C. Rinsland, and W. McMillan : Carbon monoxide distributions from the IASI/METOP mission: evaluation with other space-borne remote sensors, Atmos. Chem. Phys., 9, 8317–8330, doi:10.5194/acp-9-8317-2009, 2009.

Gielen, C., M. Van Roozendael, F. Hendrick, G. Pinardi,T. Vlemmix, V. De Bock, H. De Backer, C. Fayt, C. Hermans, D. Gillotay, and P. Wang : A simple and versatile cloud-screening method for MAX-DOAS retrievals, Atmos. Meas. Tech. Discuss., 7, 5883-5920, doi:10.5194/amtd-7-5883-2014, 2014.

Gilbert, J.-C. and C. Lemaréchal : Some numerical experiments with variable storage quasi-Newton algorithms, Math. Programming, 45, 407–435, 1989.

González Abad, G., X. Liu, K. Chance, H. Wang, T. P. Kurosu, and R. Suleiman : Updated Smithsonian Astrophysical Observatory Ozone Monitoring Instrument (SAO OMI) formaldehyde retrieval, Atmos. Meas. Tech., 8, 19–32, doi:10.5194/amt-8-19-2015, 2015.

Goodwin, J. W. L., A. G. Salway, T. P. Murrells, C. J. Dore, N. R. Passant, K. R. King, P. J. Coleman, M. M. Hobson, S. T. Pye, J. D. Watterson : UK Emissions of air pollutants 1970-1999, National Atmospheric Emissions Inventory Report, AEAT/ENV/R/0798, ISBN 1-85580-031 4., 2001, http://uk-air.defra.gov.uk/reports/empire/naei/annreport/annrep99/appdx6.pdf.

Griffiths, P. R., and J. A de Haseth : Fourier Transform Infrared Spectrometry, eds. John Wiley & Sons, Inc., Hoboke, New Jersey, 2007

Guenther, A., T. Karl, P. Harley, C. Wiedinmyer, P. I. Palmer, and C. Geron: Estimates of global terrestrial isoprene emissions using MEGAN (Model of Emissions of Gases and Aerosols from Nature), Atmos. Chem. Phys., 6, 3181–3210, 2006.

Guenther, A., X. Jiang, C. L. Heald, T. Sakulyanontvittaya, T. Duhl, L. K. Emmons, and X. Wang: The Model of Emissions of Gases and Aerosols from Nature version 2.1 (MEGAN2.1): an extended and updated framework for modeling biogenic emissions, Geosci. Model Dev., 5, 1471–1492, 2012.

Hendrick, F., J.-F. Müller, K. Clémer, P. Wang, M. De Mazière, C. Fayt, C. Gielen, C. Hermans, J. Z. Ma, G. Pinardi, T. Stavrakou, T. Vlemmix, and M. Van Roozendael : Four years of ground-based MAX-DOAS observations of HONO and NO_2 in the Beijing area, Atmos. Chem. Phys., 14, 765–781, 2014.

Hewson, W., H. Bösch, M. P. Barkley, and I. De Smedt : Characterisation of GOME-2 formaldehyde retrieval sensitivity, Atmos. Meas. Tech., 6, 371–386, doi:10.5194/amt-6-371-2013, 2013.

Hönninger, G., G. von Friedeburg, and U. Platt : Multi axis differential optical absorption spectroscopy (MAX-DOAS), Atmos. Chem. Phys., 4, 231–254, doi:10.5194/acp-4-231-2004, 2004.

Huang, X., M. Xi, J. Li, and Y. Song : A high-resolution emission inveotry of crop burning in fields in China based on MODIS thermal anomalies/fire products, Atmos. Environ., 50, 9–15, 2012.

Jenkin, M. E., T. P. Murrels, and N. R. Passant: The temporal dependence of ozone precursor emissions: estimation and application, AEA Technology, Report No. AEAT/R/ENV/0355 Issue 1, 2000.

Junkermann, W. : On the distribution of formaldehyde in the western Po-Valley, Italy, during FORMAT 2002/2003, Atmos. Chem. Phys., 9, 9187–9196, 2009.

Kleipool, Q. L., M. R. Dobber, J. F. de Haan, and P. F. Levelt : Earth surface reflectance climatology from 3 years of OMI data, J. Geophys. Res., 113(D18), D18308, doi:10.1029/2008JD010290, 2008.

Krol, M., W. Peters, P. Hooghiemstra, M. George, C. Clerbaux, D. Hurtmans, D. McInerney, F. Sedano, P. Bergamaschi, M. El Hajj, J. W. Kaiser, D. Fisher, V. Yershov, and J.-P. Muller : How much CO was emitted by the 2010 fires around Moscow? Atmos. Chem. Phys., 13, 4737–4747, doi:10.5194/acp-13-4737-2013, 2013.

Konovalov, I. B., M. Beekmann, I. N. Kuznetsova, A. Yurova, and A. M. Zvyagintsev : Atmospheric impacts of the 2010 Russian wildfires: integrating modelling and measurements of an extreme air pollution episode in the Moscow region, Atmos. Chem. Phys., 11, 10031–10056, doi:10.5194/acp-11-10031-2011, 2011.

Kurokawa, J., T. Ohara, T. Morikawa, S. Hanayama, J.-M. Greet, T. Fukui, K. Kawashima, and H. Akimoto : Emissions of air pollutants and greenhouse gases over Asian regions during 2000-2008 : Regional Emission inventory in ASia (REAS) version 2, Atmos. Chem. Phys., 13, 11019–11058, 2013.

Langford, B., P. K. Misztal, E. Nemitz, B. Davison, C. Helfter, T. A. M. Pugh, A. R. MacKenzie, S. F. Lim, and C. N. Hewitt : Fluxes and concentrations of volatile organic compounds from a South-East Asian tropical rainforest, Atmos. Chem. Phys., 10, 8391–8412, 2010.

Logan, J. A., M. J. Prather, S. C. Wofsy, and M. B. McElroy: Tropospheric chemistry: A global perspective, J. Geophys. Res., 86, 7210–7254, 1981.

MacDonald, S. M., H. Oetjen, A. S. Mahajan, L. K. Whalley, P. M. Edwards, D. E. Heard, C. E. Jones, and J. M. C. Plane : DOAS measurements of formaldehyde and glyoxal above a south-east Asian tropical rainforest, Atmos. Chem. Phys., 12, 5949–5962, doi:10.5194/acp-12-5949-2012, 2012.

Marais, E. A., D. J. Jacob, T. P. Kurosu, K. Chance, J. G. Murphy, C. Reeves, G. Mills, S. Casadio, D. B. Millet, M. P. Barkley, F. Paulot, and J. Mao : Isoprene emissions in Africa inferred from OMI observations of formaldehyde columns, Atmos. Chem. Phys., 12, 6219–6235, doi:10.5194/acp-12-6219-2012, 2012.

Marais, E. A., D. J. Jacob, A. Guenther, K. Chance, T. P. Kurosu, J. G. Murphy, C. E. Reeves, and H. O. T. Pye : Improved model of isoprene emissions in Africa using Ozone Monitoring Instrument (OMI) satellite observations of formaldehyde: implications for oxidants and particulate matter, Atmos. Chem. Phys., 14, 7693–7703, doi:10.5194/acp-14-7693-2014, 2014.

Marengo, J. A., C. Nobre, J. Tomasella, M. Oyama, G. Sampaio de Oliveira, R. de Oliveira, H. Camargo, L. Alves, and I. F. Brown : The Drought of Amazonia in 2005. J. Climate 21 (3): 495–516, doi:10.1175/2007JCLI1600.1, 2008.

Marengo, J. A., J. Tomasella, L. M. Alves, W. R. Soares, and D. A. Rodriguez : The drought of 2010 in the context of historical droughts in the Amazon region, Geophys. Res. Lett., 38 (12), doi: 10.1029/2011GL047436, 2011.

Martin, R. V, K. V. Chance, D. J. Jacob, T. P. Kurosu, R. J. D. Spurr, E. J. Bucsela, J. Gleason, P. I. Palmer, I. Bey, A. M. Fiore, Q. Li, R. M. Yantosca, and R. B. A. Koelemeijer : An improved retrieval of tropospheric nitrogen dioxide from GOME, J. Geophys. Res., 107(D20), doi:10.1029/2001JD001027, 2002.

Millet, D. B., D. J. Jacob, S. Turquety, R. C. Hudman, S. Wu, A. Fried, J. Walega, B. G. Heikes, D. R. Blake, H. B. Singh, B. E. Anderson, and A. D. Clarke : Formaldehyde distribution over North America: Implications for satellite retrievals of formaldehyde columns and isoprene emission, J. Geophys. Res. 111, D24S02, doi:10.1029/2005JD006853, 2006.

Millet, D. B., D. J. Jacob, K. F. Boersma, T. Fu, T. P. Kurosu, K. Chance, C. L. Heald, and A. Guenther : Spatial distribution of isoprene emissions from North America derived from formaldehyde columns measurements by the OMI satellite sensor, J. Geophys. Res., 113, D02307, doi:10.1029/2007JD008950, 2008.

Millet, D. B., A. Guenther, D. A. Siegel, N. B. Nelson, H. B. Singh, J. A. de Gouw, C. Warneke, J. Williams, G. Eerdekens, V. Sinha, T. Karl, F. Flocke, E. C. Apel, D. D. Riemer, P. I. Palmer, and M. Barkley: Global atmospheric budget of acetaldehyde: 3-D model analysis and constraints from in-situ and satellite observations, Atmos. Chem. Phys., 10, 3405–3425, 2010.

Mu, M, J. T. Randerson, G. R. van der Werf, L. Giglio, P. Kasibhatla, D. Morton, G. J. Collatz, R. S. DeFries, E. J. Hyer, E. M. Prins, D. W. T. Griffith, D. Wunch, G. C. Toon, V. Sherlock, and P. O. Wennberg : Daily and 3-hourly variability in global fire emissions and consequences for atmospheric model predictions of carbon monoxide, J. Geophys. Res., 116, D24303, doi:10.1029/2011JD016245, 2011.

Müller, J.-F., and G. Brasseur: IMAGES: A three-dimensional chemical transport model of the global troposphere, J. Geophys. Res., 100, 16445–16490, 1995.

Müller, J.-F., and T. Stavrakou: Inversion of CO and NOx emissions using the adjoint of the IMAGES model, Atmos. Chem. Phys., 5, 1157–1186, 2005.

Müller, J.-F., T. Stavrakou, S. Wallens. I. De Smedt, M. Van Roozendael, J. Rinne, B. Munger, A. Goldstein, and A. Guenther: Global isoprene emissions estimated using MEGAN, ECMWF analyses and a detailed canopy environmental model, Atmos. Chem. Phys., 8, 1329–1341, 2008.

Palmer, P. I., D. J. Jacob, A. Fiore, R. V. Martin, K. V. Chance, T. P. Kurosu, I. Bey, R. Yantosca : Air mass factor formulation for spectroscopic measurements from satellites: Application to formaldehyde retrievals from the Global Ozone Monitoring Experiment, J. Geophys. Res., 106(D13), 14539–14550, doi:10.1029/2000JD900772, 2001.

Palmer, P. I., D. J. Jacob, A. Fiore, K. V. Chance, R. V. Martin,T. P. Kurosu, I. Bey, R. Yantosca, A. Fiore, and Q. Li : Mapping isoprene emissions over North America using formaldehyde column observations from space, J. Geophys. Res., 108(D6), 4180, doi:10.1029/2002JD002153, 2003.

Palmer, P. I. D. S. Abbot, T.-M. Fu, D. J. Jacob, K. Chance, T. P. Kurosu, A. Guenther, C. Wiedinmyer, J. C. Stanton, M. J. Pilling, S. N. Pressley, B. Lamb, and A. L. Sumner, Quantifying the seasonal and interannual variability of North American isoprene emissions using satellite observations of the formaldehyde column, J. Geophys. Res. 111, D12315, doi:10.1029/2005JD006689, 2006.

Peeters, J., T. L. Nguyen, and L. Vereecken: HOx radical regeneration in the oxidation of isoprene, Phys. Chem. Chem. Phys., 11, 5935–5939, 2009.

Peeters, J., and J.-F. Müller : HOx radical regeneration in isoprene oxidation via peroxy radical isomerisations. II: Experimental evidence and global impact, Phys. Chem. Chem. Phys., 12(42), 14227–14235, doi:10.1039/C0CP00811G, 2010.

Peeters, J., J.-F. Müller, T. Stavrakou, and S. V. Nguyen : Hydroxyl radical recycling in isoprene oxidation driven by hydrogen bonding and hydrogen tunneling : the upgraded LIM1 mechanism, J. Phys. Chem. A, 118 (38), 8625–8643, doi: 10.1021/jp5033146, 2014.

Peters, E., F. Wittrock, K. Großmann, U. Frieß, A. Richter, and J. P. Burrows : Formaldehyde and nitrogen dioxide over the remote western Pacific Ocean: SCIAMACHY and GOME-2 validation using ship-based MAX-DOAS observations, Atmos. Chem. Phys., 12, 11179–11197, doi:10.5194/acp-12-11179-2012, 2012.

Pinardi, G., M. Van Roozendael, N. Abuhassan, C. Adams, A. Cede, K. Clémer, C. Fayt, U. Friess, M. Gil, J. Herman, C. Hermans, F. Hendrick, H. Irie, A. Merlaud, M. Navarro Comas, E. Peters, A. J. M. Piters, O. Puentedura, A. Richter, A. Schönhardt, R. Shaiganfar, E. Spinei, K. Strong, H. Takashima, M. Vrekoussis, T. Wagner, F. Wittrock, and S. Yilmaz : MAX-DOAS formaldehyde slant column measurements during CINDI: intercomparison and analysis improvement, Atmos. Meas. Tech., 6(1), 167-185, doi:10.5194/amt-6-167-2013, 2013.

Platt, U. and J. Stutz : Differential Absorption Spectroscopy, Physics of Earth and Space Environments, eds. Springer-Verlag Berlin, Heidelberg, doi:10.1007/978-3-540-75776-4, 2008.

R'Honi1, Y., L. Clarisse, C. Clerbaux, D. Hurtmans, V. Duflot, S. Turquety, Y. Ngadi, and P.-F. Coheur : Exceptional emissions of NH_3 and HCOOH in the 2010 Russian wildfires, Atmos. Chem. Phys., 13, 4171–4181, doi:10.5194/acp-13-4171-2013, 2013.

Richter, A., M. Begoin, A. Hilboll, and J. P. Burrows : An improved NO_2 retrieval for the GOME-2 satellite instrument, Atmos. Meas. Tech., 4, 1147–1159, 2011.

Roberts, G., M. J. Wooster, and E. Lagoudakis : Annual and diurnal african biomass burning temporal dynamics, Biogeosciences, 6, 849–866, 2009.

Saide, P. E., J. Kim, C. H. Song, M. Choi, Y. Cheng, and G. R. Carmichael : Assimilation of next generation geostationary aerosol optical depth retrievals to improve air quality simulations, Geophys. Res. Lett., 41, 9188–9196, doi:10.1002/2014GL062089, 2014.

Sander, S. P., J. Abbatt, J. R. Barker, J. B. Burkholder, R. R. Friedl, D. M. Golden, R. E. Huie, C. E. Kolb, M. J. Kurylo, G. K. Moortgat, V. L. Orkin and P. H. Wine : Chemical Kinetics and Photochemical Data for Use in Atmospheric Studies, Evaluation No. 17, JPL Publication 10-6, Jet Propulsion Laboratory, Pasadena, 2011 http://jpldataeval.jpl.nasa.gov.

Saunders, S. M., M. E. Jenkin, R. G. Derwent, and M. J. Pilling : Protocol for the development of the Master Chemical Mechanism, MCM v3 (Part A): tropospheric degradation of nonaromatic volatile organic compounds, Atmos. Chem. Phys., 3, 161–180, 2003.

Schultz, M. G, A. Heil, J. J. Hoelzemann, A. Spessa, K. Thonicke, J. Goldammer, A. C. Held, J. M. Pereira : Global Emissions from Wildland Fires from 1960 to 2000, Global Biogeochem. Cycles, 22, GB2002, doi:10.1029/2007GB003031, 2008.

Singh, H. B., W. H. Brune, J. H. Crawford, D. J. Jacob, and P. B. Russell : Overview of the summer 2004 Intercontinental Chemical Transport Experiment North America (INTEX-A), J. Geophys. Res., 111(D6), D24S01, doi:10.1029/2006JD007905, 2006.

Sofiev, M., T. Ermakova, and R. Vankevich : Evaluation of the smoke injection height from wild-land fires using remote sensing data, Atmos. Phys. Chem., 12, 1995–2006, 2012.

Sofiev, M., R. Vankevich, T. Ermakova, and J. Hakkarainen : Global mapping of maximum emission heights and resulting vertical profiles of wildfire emissions, Atmos. Chem. Phys., 13, 7039-7052, 2013.

Spurr, R. J. D. : LIDORT and VLIDORT: Linearized pseudo-spherical scalar and vector discrete ordinate radiative transfer models for use in remote sensing retrieval problems, in Light Scattering Reviews, edited by A. Kokhanovsky, pp. 229-271, Berlin, 2008.

Stammes, P., M. Sneep, J. F. de Haan, J. P. Veefkind, P. Wang, and P. F. Levelt : Effective cloud fractions from the Ozone Monitoring Instrument: Theoretical framework and validation, J. Geophys. Res., 113(D16), D16S38, doi:10.1029/2007JD008820, 2008.

Stavrakou, T., J.-F. Müller, I. De Smedt, M. Van Roozendael, G.

van der Werf, L. Giglio, and A. Guenther : Evaluating the performance of pyrogenic and biogenic emission inventories against one decade of space-based formaldehyde columns, Atmos. Chem. Phys., 9, 1037–1060, 2009a.

Stavrakou, T., J.-F. Müller, I. De Smedt, M. Van Roozendael, G. van der Werf, L. Giglio, and A. Guenther : Global emissions of non-methane hydrocarbons deduced from SCIAMACHY formaldehyde columns through 2003-2006, Atmos. Chem. Phys., 9, 3663-3679, 2009b.

Stavrakou, T., J.-F. Müller, I. De Smedt, M. Van Roozendael, M. Kanakidou, M. Vrekoussis, F. Wittrock, A. Richter, and J. P. Burrows: The continental source of glyoxal estimated by the synergistic use of spaceborne measurements and inverse modelling, Atmos. Chem. Phys., 9, 8431–8446, 2009c.

Stavrakou, T., J. Peeters, and J.-F. Müller : Improved global modelling of HOx recycling in isoprene oxidation : evalaution against the GABRIEL and INTEX-A aircraft campaign measurements, Atmos. Chem. Phys., 10, 9863–9878, 2010.

Stavrakou, T., A. Guenther, A. Razavi, L. Clarisse, C. Clerbaux, P.-F. Coheur, D. Hurtmans, F. Karagulian, M. De Mazière, C. Vigouroux, C. Amelynck, N. Schoon, Q. Laffineur, B. Heinesch, M. Aubinet, C. Rinsland, and J.-F. Müller: First space-based derivation of the global atmospheric methanol emission fluxes, Atmos. Chem. Phys., 11, 4873–4898, 2011.

Stavrakou, T., J.-F. Müller, K-F. Boersma, R.J. van der A, J. Kurokawa, T. Ohara, and Q. Zhang: Key chemical NOx sink uncertainties and how they influence top-down emissions of nitrogen oxides, Atmos. Chem. Phys., 13, 9057–9082, 2013.

Stavrakou, T., J.-F. Müller, M. Bauwens, I. De Smedt, M. Van Roozendael, A. Guenther, M. Wild, and X. Xia : Isoprene emissions over Asia 1979-2012 : impact of climate and land use changes, Atmos. Chem. Phys., 14, 4587–4605, 2014.

Takahashi, H. G., H. Fujinami, T. Yasunari, and J. Matsumoto : Diurnal rainfall pattern observed by Tropical Rainfall Measuring Mission Precipitation Radar (TRMM-PR) around the Indochina peninsula, J. Geophys. Res., 115, D07109, doi:10.1029/2009JD012155, 2010.

van der Werf, G. R., J. T. Randerson, L. Giglio, G. J. Collatz, M. Mu, P. S. Kasibhatla, D. C. Morton, R. S. DeFries, Y. Jin, and T. T. van Leeuwen: Global fire emissions and the contribution of deforestation, savanna, forest, agricultural, and peat fires (1997–2009), Atmos. Chem. Phys., 10, 11707–11735, 2010.

Valks, P. J. M., G. Pinardi, A. Richter, J. C. Lambert, N. Hao, D. Loyola, M. Van Roozendael, and S. Emmadi : Operational total and tropospheric NO_2 column retrieval for GOME-2, Atmos. Meas. Tech., 4(7), 1491–1514, doi:10.5194/amt-4-1491-2011, 2011.

Vigouroux, C., F. Hendrick, T. Stavrakou, B. Dils, I. De Smedt, C. Hermans, A. Merlaud, F. Scolas, C. Senten, G. Vanhaelewyn, S. Fally, M. Carleer, J.-M. Metzger, J.-F. Müller, M. Van Roozendael, and M. De Mazière : Ground-based FTIR and MAX-DOAS observations of formaldehyde at Réunion Island and comparisons with satellite and model data, Atmos. Chem. Phys., 9(4), 15891-15957, doi:10.5194/acp-9-9523-2009, 2009.

Vlemmix, T., F. Hendrick, G. Pinardi, I. De Smedt, C. Fayt, C. Hermans, A. Piters, P. Levelt, and M. Van Roozendael : MAX-DOAS observations of aerosols, formaldehyde and nitrogen dioxide in the Beijing area: comparison of two profile retrieval approaches, Atmos. Meas. Tech., 8, 941–963, doi:10.5194/amt-8-941-20157, 2015.

Wang, P., P. Stammes, R. J. van der A, G. Pinardi, and M. Van Roozendael : FRESCO+: an improved O_2 A-band cloud retrieval algorithm for tropospheric trace gas retrievals, Atmos. Chem. Phys., 8, 6565–6576, doi:10.5194/acp-8-6565-2008, 2008.

Wiedinmyer, C., S. Akagi, R. J. Yokelson, L. K. Emmons, J. A. Al-Saadi, J. J. Orlando, A. J. Soja : The Fire INventory from NCAR (FINN): a high resolution global model to estimate the emissions from open burning, Geosci. Model Dev., 4, 625–641, doi:10.5194/gmd-4-625-2011, 2011.

Yamaji, K., J. Li, I. Uno, Y. Kanaya, H. Irie, M. Takigawa, Y. Komazaki, P. Pochanart, Y. Liu, H. Tanimoto, T. Ohara, X. Yan, Z; Wang, and H. Akimoto: Impact of open crop residual burning on air quality over Central Eastern China during the Mount Tai Experiment 2006 (MTX2006), Atmos. Chem. Phys., 10, 7353–7368, 2010.

Yurganov, L. N., V. Rakitin, A. Dzhola, T. August, E. Fokeeva, M. George, G. Gorchakov, E. Grechko, S. Hannon, A. Karpov, L. Ott, E. Semutnikova, R. Shumsky, and L. Strow : Satellite- and ground-based CO total column observations over 2010 Russian fires: accuracy of top-down estimates based on thermal IR satellite data, Atmos. Chem. Phys., 11, 7925-7942, doi:10.5194/acp-11-7925-2011, 2011.

Zhu, L., D. J. Jacob, L. J. Mickley, E. A. Marais, D. S. Cohan, Y. Yoshida, B. N Duncan, G. González Abad, and K. V. Chance : Anthropogenic emissions of highly reactive volatile organic compounds in eastern Texas inferred from oversampling of satellite (OMI) measurements of HCHO columns,

Table 1. Model simulations conducted to investigate the diurnal cycle of HCHO columns (Sect. 3).

Name	Description
STD	Standard forward simulation
NBB	neglect biomass burning emissions
NDC	neglect the diurnal cycle of emissions
NDCBL	neglect diurnal cycle of boundary layer mixing
NDCC	neglect diurnal cycle of deep convection

Table 2. Performed flux inversions.

Name	Description
GOME-2	Use GOME-2 data
OMI	Use OMI data
OMI-DE	Doubled a priori errors on the emission fluxes
OMI-HE	Halved a priori errors on the emission fluxes
OMI-CF	Use only OMI data with cloud fraction < 0.2
OMI-IS	Ignore isomerization of isoprene peroxy radicals

Table 3. A priori and top-down VOC emissions (Tg/yr) by region. The emission inversions are defined in Table 2. The regions are defined as follows. North America : US and Canada, Southern America : Mexico, Central and South America, Northern (Southern) Africa : north (south) of the equator, Tropics : 25 S-25 N, Southeastern US : 25-38 N, 60-100 W, Amazonia : 14 S-10 N, 45-80 W, Indonesia : 10 S-6 N, 95-142.5 E, Indochina : 6-22 N, 97.5-110 E, Europe extends to Urals (55 E), FSU=Former Soviet Union.

Biomass burning (TgVOC/yr)	A priori	GOME-2	OMI	OMI-DE	OMI-HE	OMI-CF	OMI-IS
North America	5.3	3.6	3.3	5.3	2.9	4.6	3.2
Southern America	36.9	20.7	17.1	16.8	17.8	16.4	16.2
Amazonia	26.5	13.0	10.4	10.2	10.8	10.0	9.7
Northern Africa	14.9	8.6	8.8	8.8	9.2	9.7	8.1
Southern Africa	25.8	17.6	23.8	24.6	23.0	25.5	23.1
Indochina	6.2	4.6	5.3	5.6	4.7	5.6	5.0
Tropics	93.3	56.8	60.6	61.6	60.4	63.0	57.8
Extratropics	12.0	10.0	9.9	13.4	8.8	12.1	9.2
Global	105.4	67.0	70.5	74.9	69.1	75.1	67.1
Isoprene (Tg/yr)	A priori	GOME-2	OMI	OMI-DE	OMI-HE	OMI-CF	OMI-IS
Europe (excl. FSU)	3.8	3.3	3.8	3.7	3.4	3.9	3.7
Europe	7.4	6.9	8.2	8.8	7.7	8.6	8.1
North America	34.7	26.5	29.9	28.0	31.9	30.4	28.6
Southeastern US	14.5	8.9	10.8	9.8	12.2	11.3	9.9
Southern America	149.5	142.1	121.2	115.9	128.9	125.6	114.0
Amazonia	99.4	92.5	73.7	69.1	80.6	77.2	67.9
Northern Africa	50.6	45.3	43.7	40.4	46.8	44.7	41.5
Southern Africa	31.0	31.3	31.5	32.8	31.0	34.2	30.7
Indonesia	11.6	10.3	11.1	10.5	11.4	10.6	10.9
Indochina	7.6	7.1	7.5	7.3	7.5	7.4	7.3
Tropics	314.8	291.1	272.3	261.9	286.2	281.3	260.2
Extratropics	48.3	39.4	44.7	44.1	45.8	46.4	43.3
Global	363.1	330.5	317.0	305.9	332.1	327.8	303.5
Anthropogenic (TgVOC/yr)	A priori	GOME-2	OMI	OMI-DE	OMI-HE	OMI-CF	OMI-IS
Global	155.6	138.6	157.5	162.0	154.2	163.4	155.8

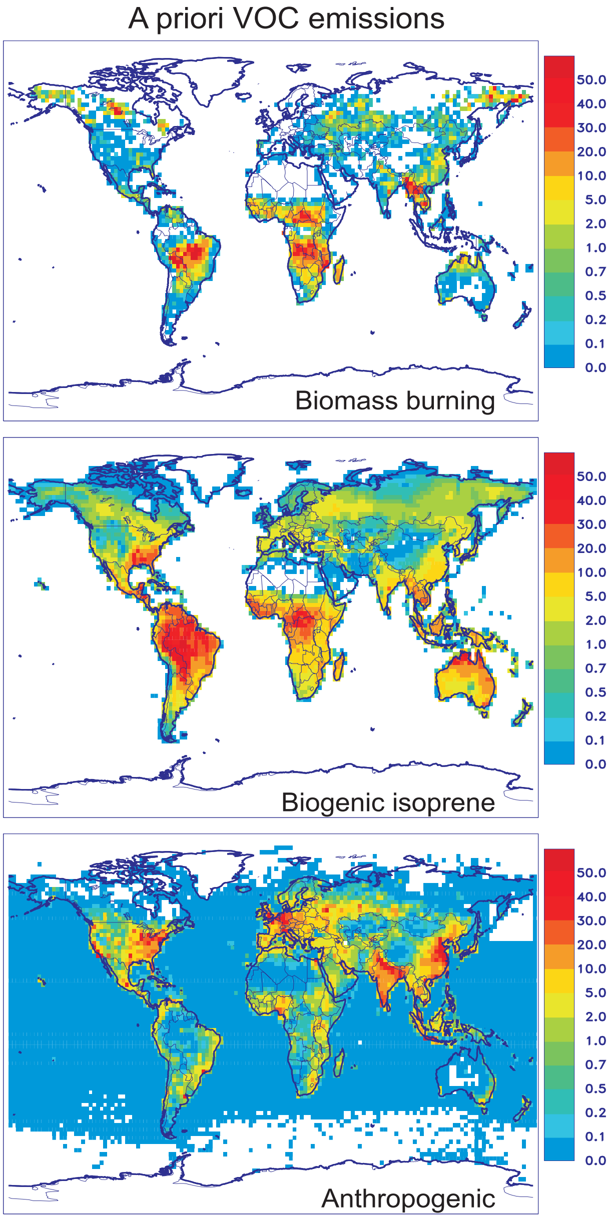

Fig. 1. A priori annually averaged pyrogenic NMVOC, biogenic isoprene and anthropogenic NMVOC emissions used in the CTM. Units are 10^{10} molec.cm^{-2} s^{-1}.

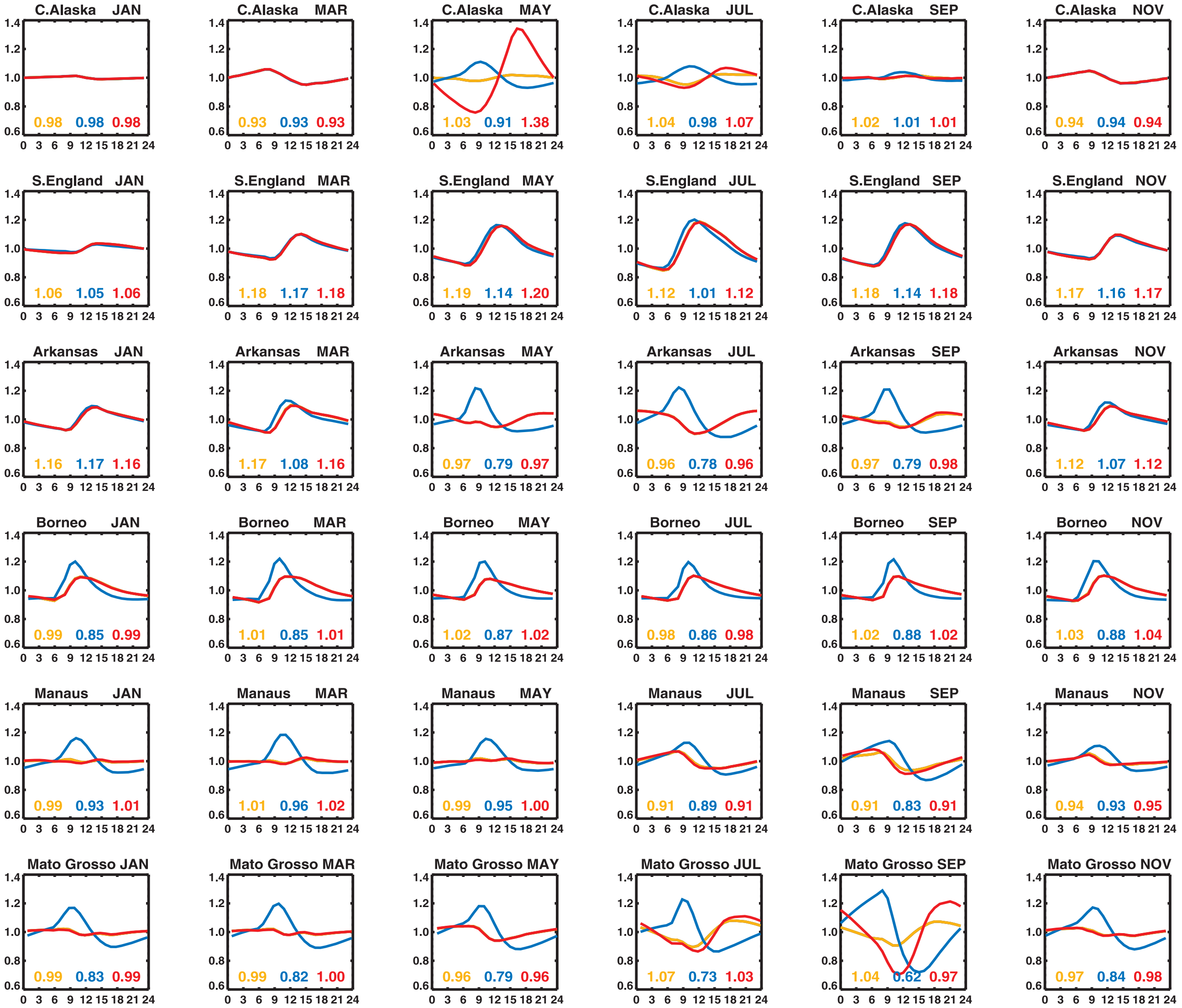

Fig. 2. Modelled diurnal variations of HCHO columns (normalized at noon) at six locations, Central Alaska (65 N, 151 W), South England (51 N, 2.5 W), Arkansas (35 N, 91 W), Borneo (4 N, 117 E), Manaus (3 S, 61 W), and Mato Grosso (9 S, 51 W) in January, March, May, July, September and November 2010. The simulations STD, NBB, and NDC of Table 1 are shown in red, orange and blue, respectively. The modelled ratios of 13h30 LT to 9h30 LT columns are given inside each panel.

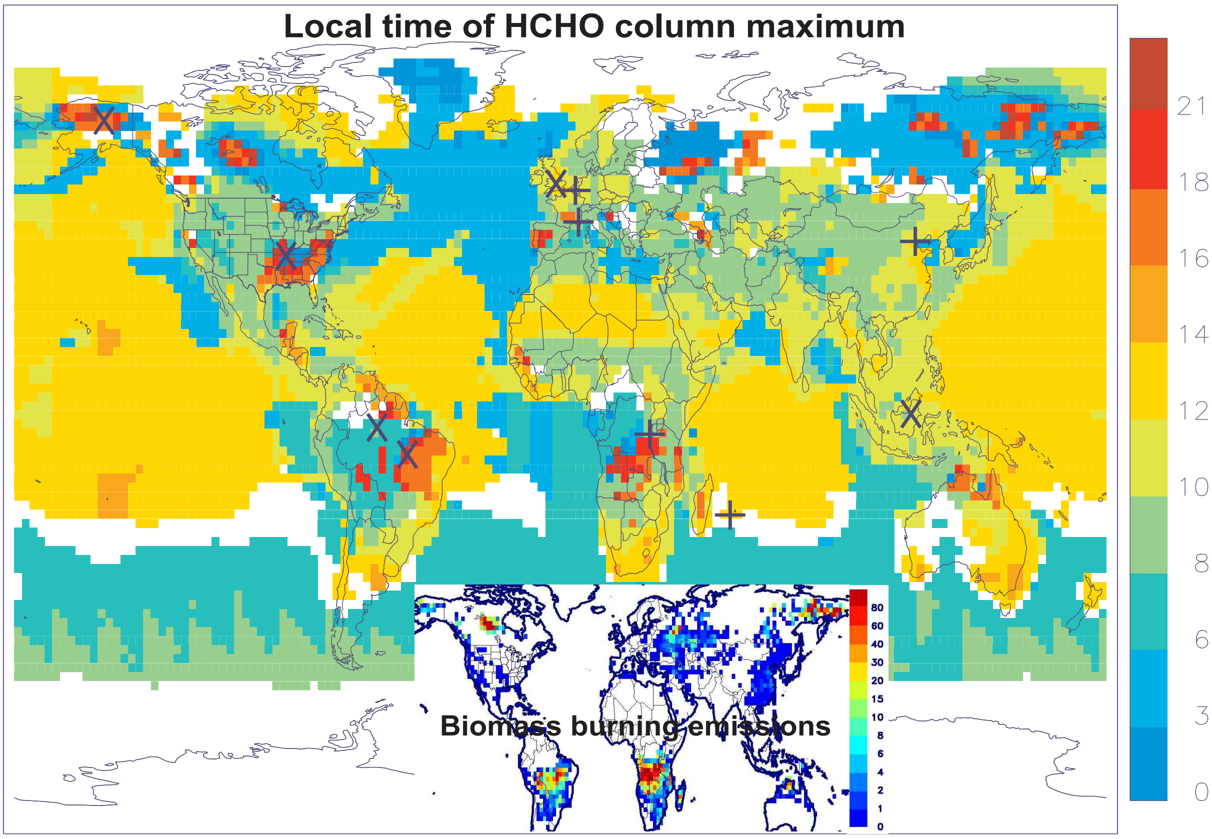

Fig. 3. Modelled local time (in hour) of the maximum in HCHO column, for July 2010. The locations of sites for which comparisons are shown in Fig. 2 and Fig. 4-5 are shown as crosses (x) and plus symbols (+), respectively. White color represents regions with diurnal variability of less than 5%. The distribution of open fire NMVOC emissions (10^{10} molec.cm^{-2} s^{-1}) for the same month is also shown inset.

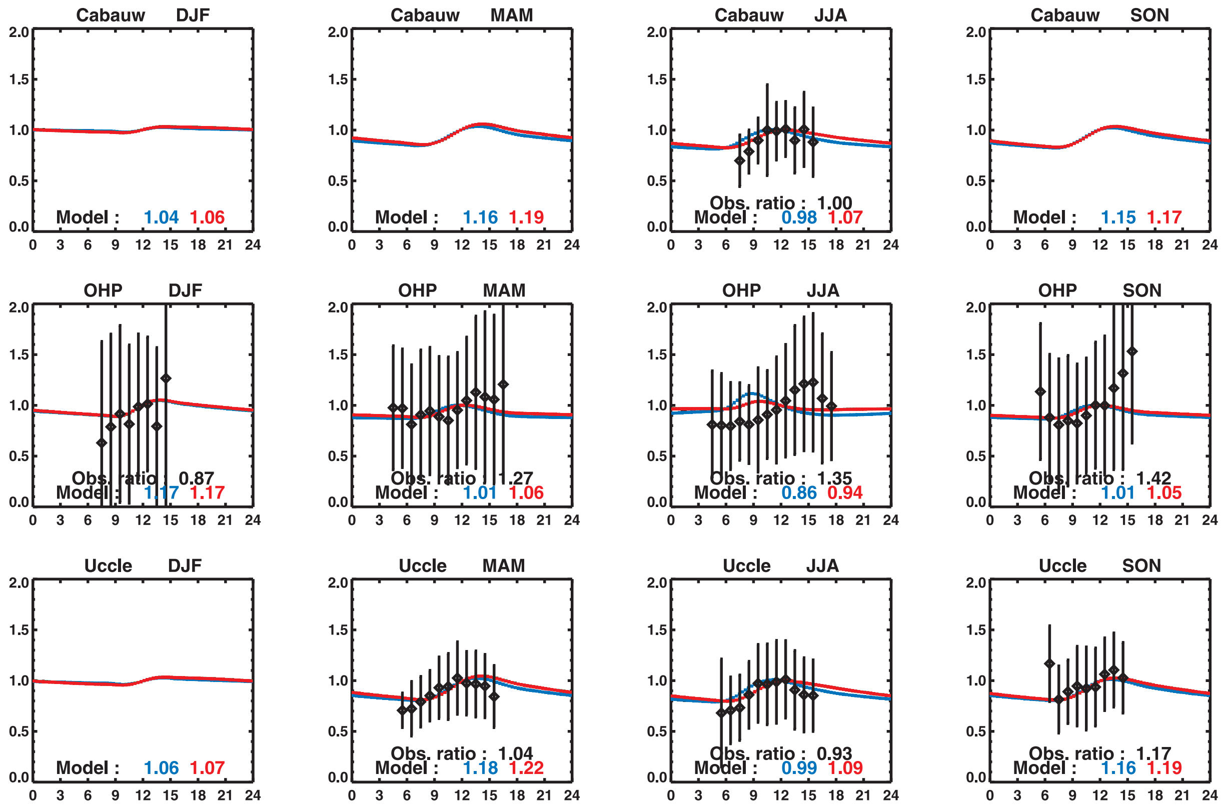

Fig. 4. Seasonally averaged observed (black) and modelled (red) diurnal variations of HCHO columns normalized at noon at 3 European sites, Cabauw, Observatoire de Haute Provence, and Uccle. The observed columns are obtained using the MAX-DOAS technique (Sect. 3). The errors bars correspond to the measurement standard deviation. Modelled columns calculated assuming no diurnal emission variability are shown in blue. The observed and modelled ratios (blue and red) of 13h30 LT to 9h30 LT columns are given inset.

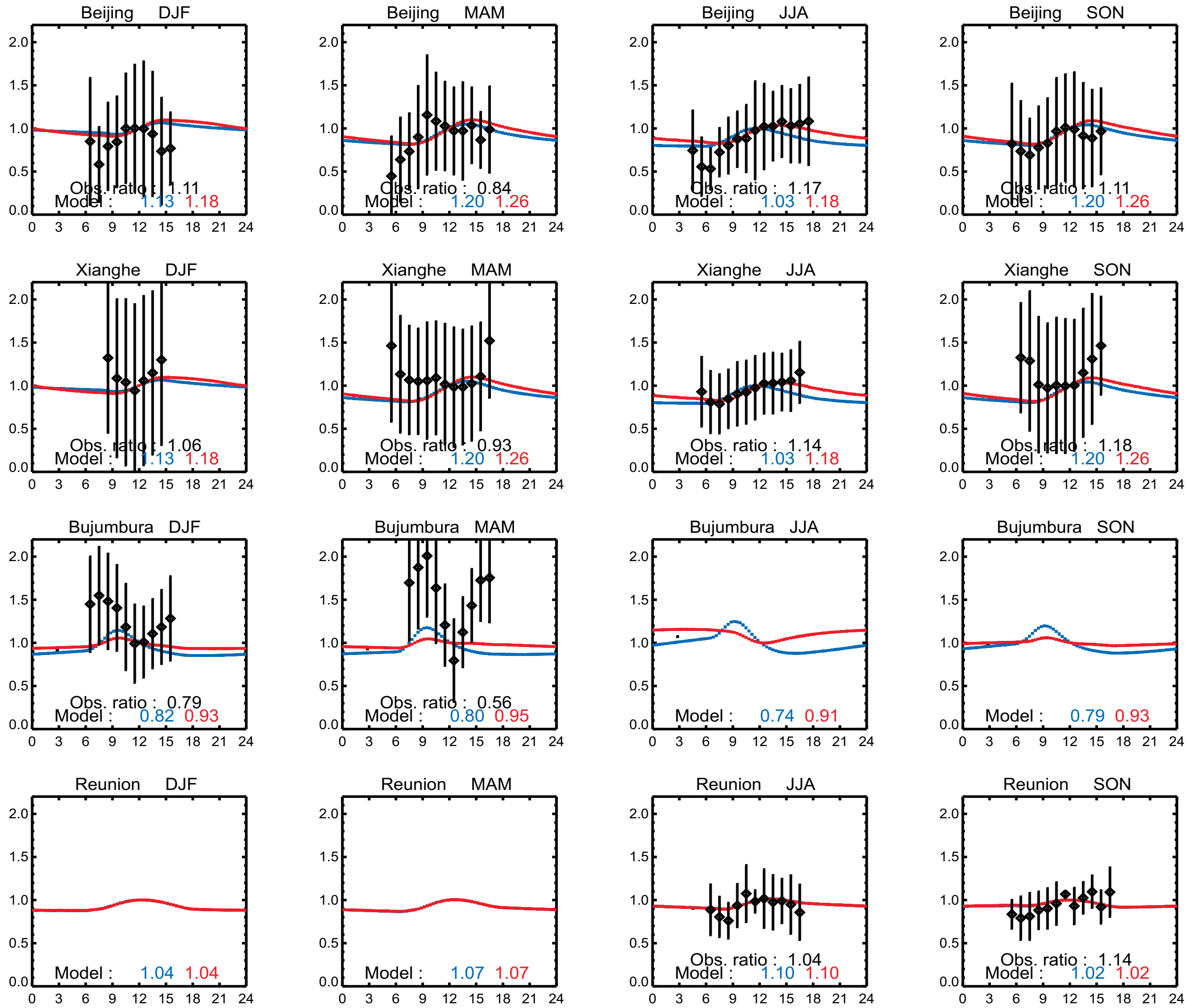

Fig. 5. As in Fig. 4, comparison between modelled and observed diurnal variations for four sites : Beijing, Xianghe, Bujumbura and Reunion Island. The observations were obtained using the MAX-DOAS (Beijing, Xianghe, Bujumbura) and FTIR (Reunion Island) techniques.

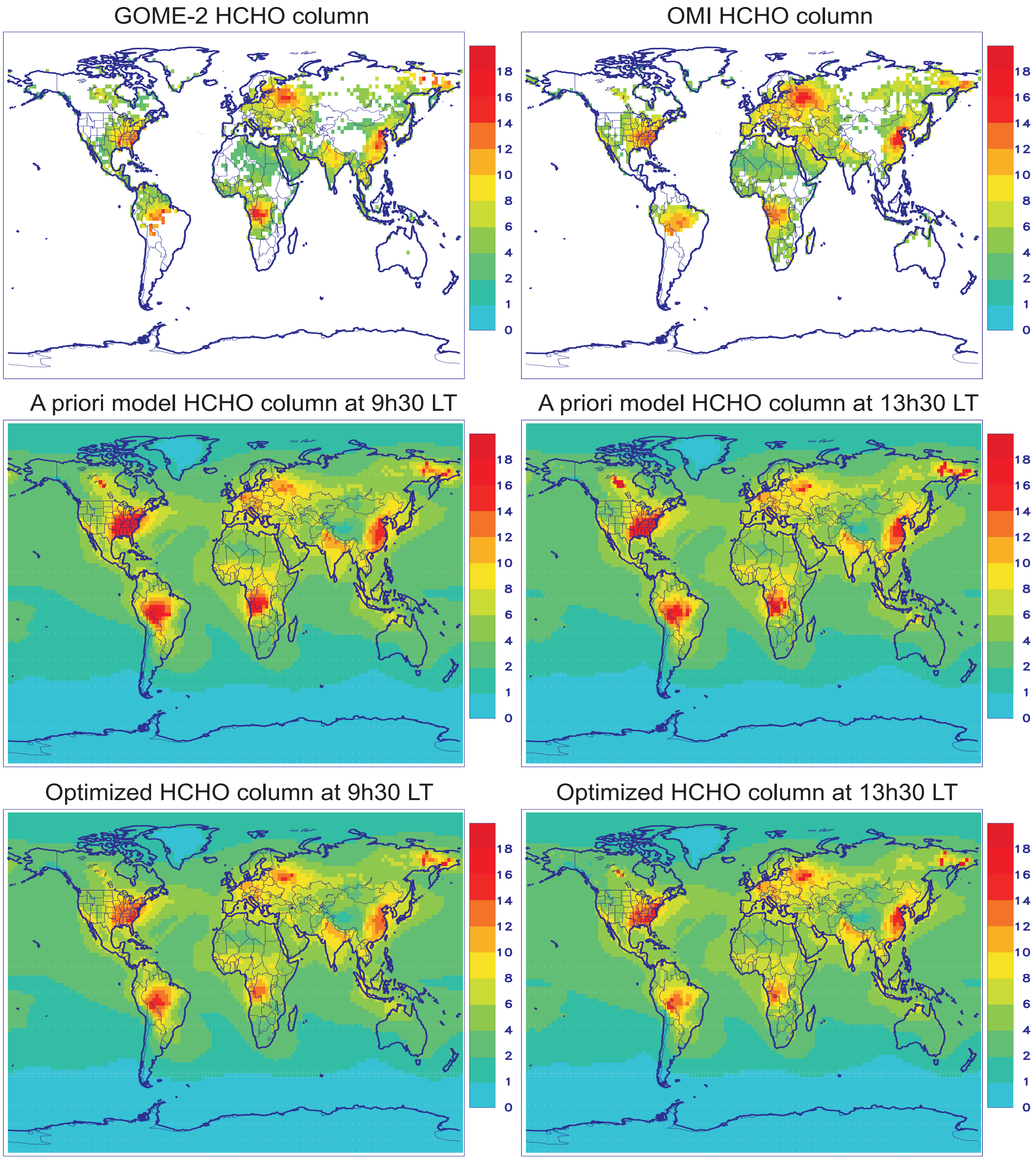

Fig. 6. Observed (upper panels) HCHO columns by GOME-2 and OMI instruments in July 2010. Simulated HCHO columns using IMAGESv2 CTM at the overpass times of GOME-2 and OMI (middle panels), and optimized modelled columns derived from the inversions using GOME-2 data (left) and OMI columns (right). The columns are expressed in 10^{15} molec.cm^{-2}.

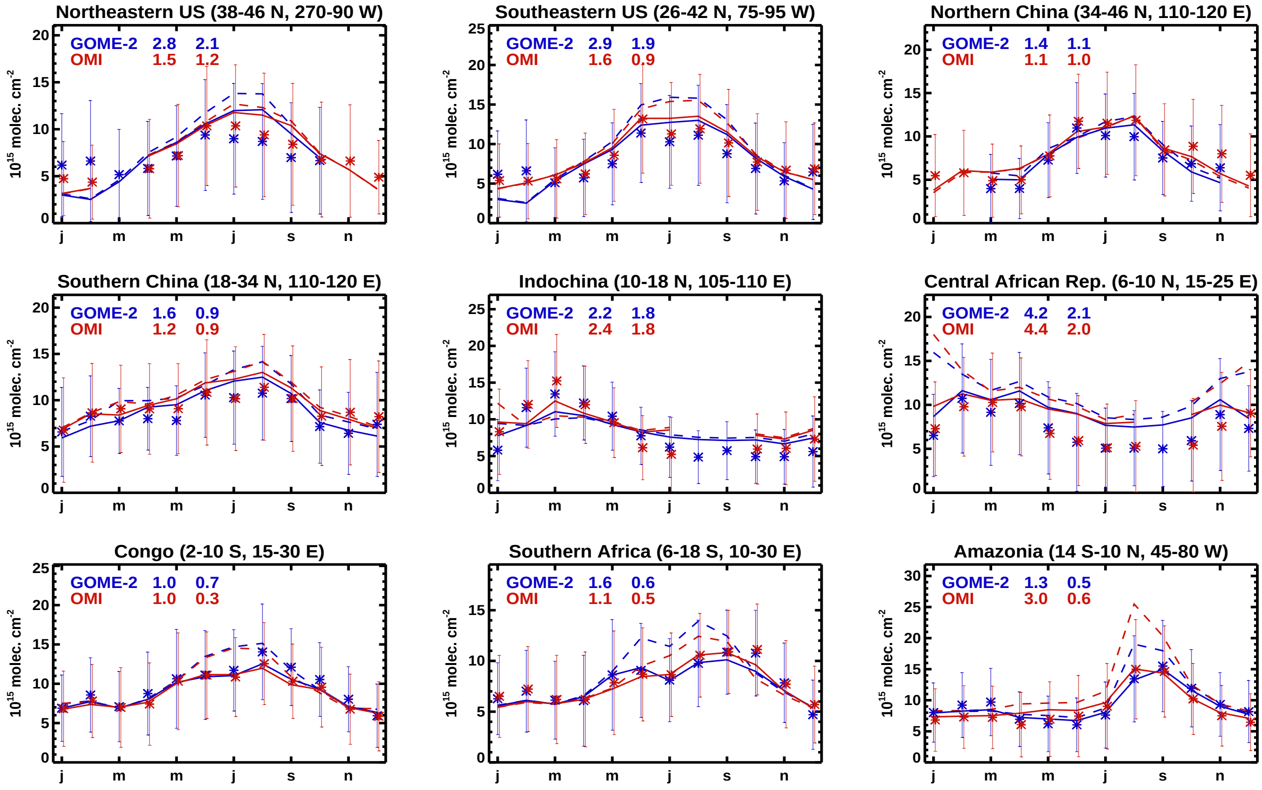

Fig. 7. Monthly averages of observed GOME-2 (blue asterisks) and OMI (red asterisks) HCHO columns and modelled columns over nine selected regions. Dashed and solid lines correspond to a priori and optimized model columns, respectively, calculated at 9h30 LT (in blue) and at 13h30 LT (in red). The units are 10^{15} molec.cm^{-2}. The mean absolute deviation between the a priori (left) and optimized (right) modelled and the observed columns is given inset each panel (in blue for GOME-2, in red for OMI). Error bars (blue for GOME-2, red for OMI) represent the retrieval error provided for each dataset.

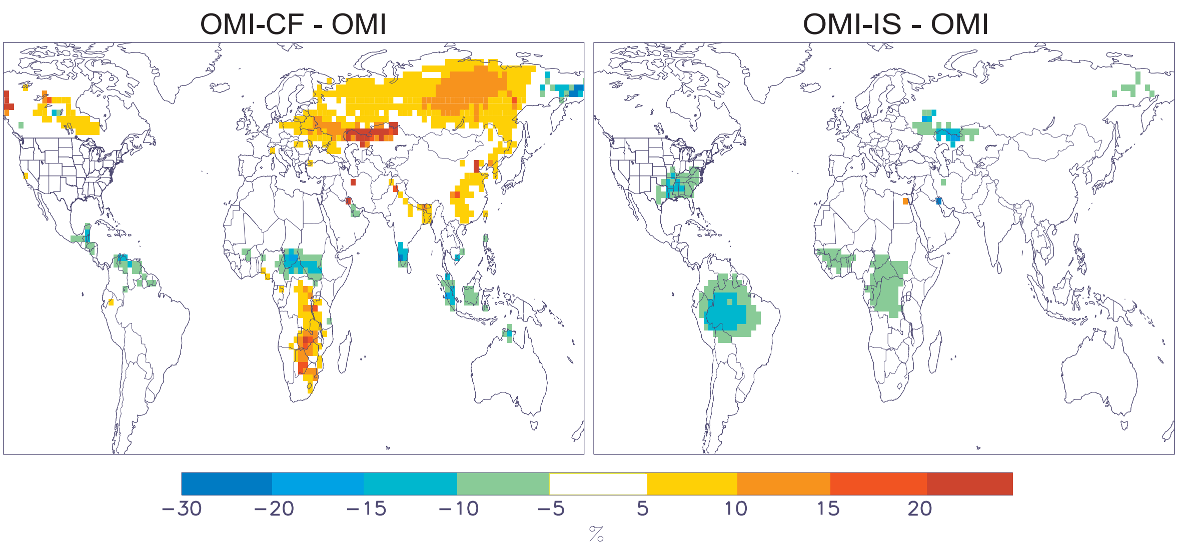

Fig. 8. Percentage difference of the total VOC emissions inferred by the sensitivity inversions (OMI-CF, left panel and OMI-IS, right panel) and the standard OMI inversion for the month of July (see Table 2).

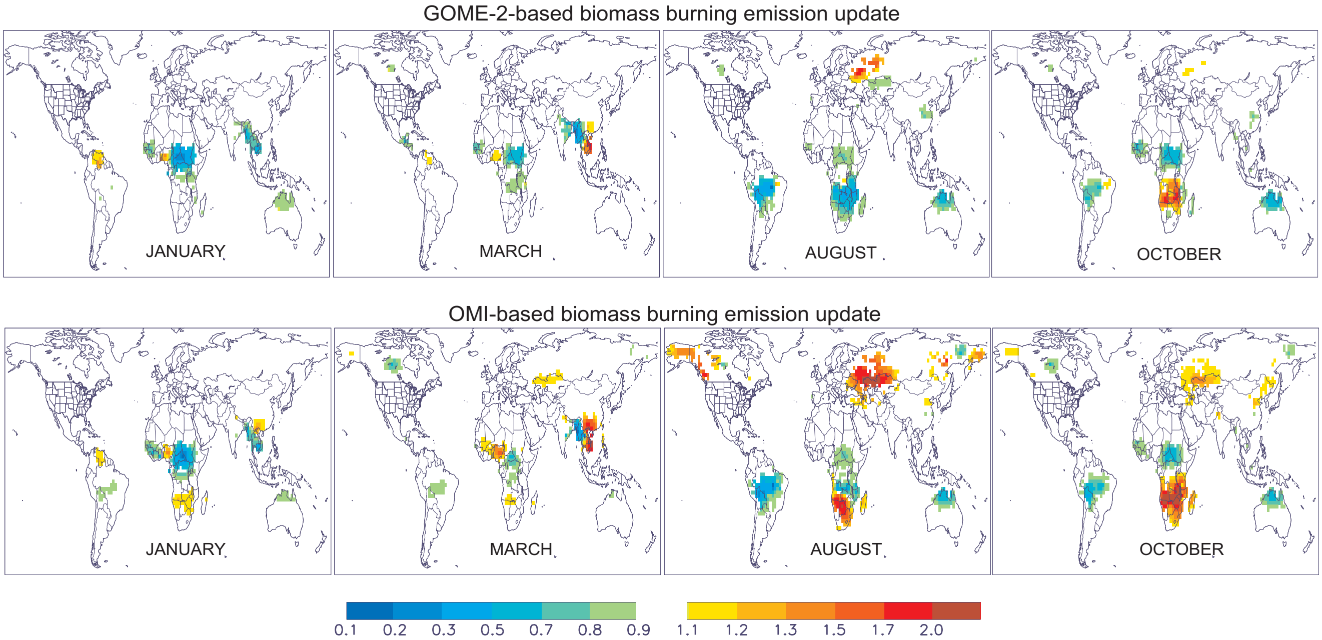

Fig. 9. Ratios of optimized to a priori pyrogenic VOC fluxes derived by source inversion of HCHO columns from GOME-2 (upper panels) and OMI (lower panels) in January, March, August and October 2010. Ratio values comprised between 0.9 and 1.1 are not shown for the sake of clarity.

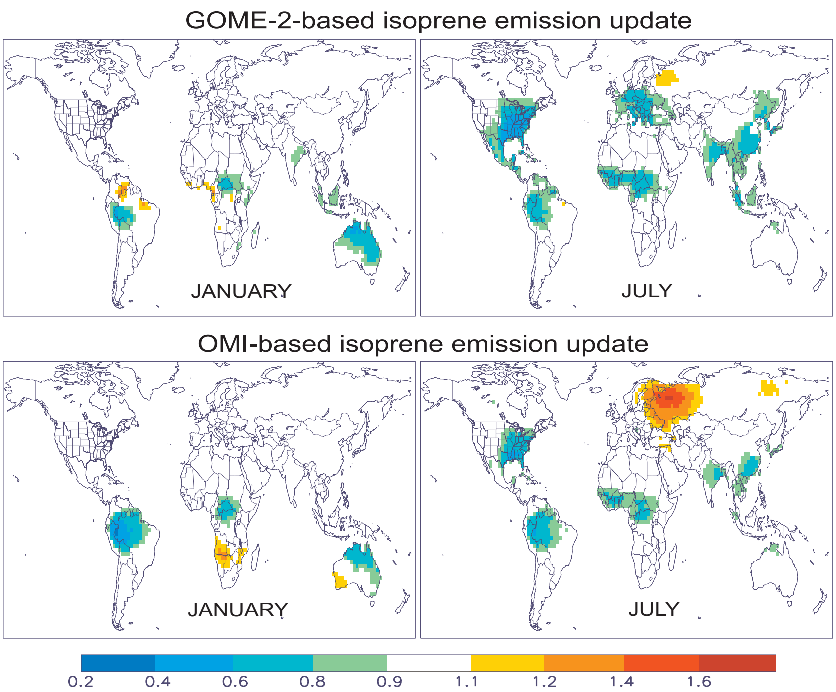

Fig. 10. Same as Fig. 9, but for isoprene emissions in January and July.

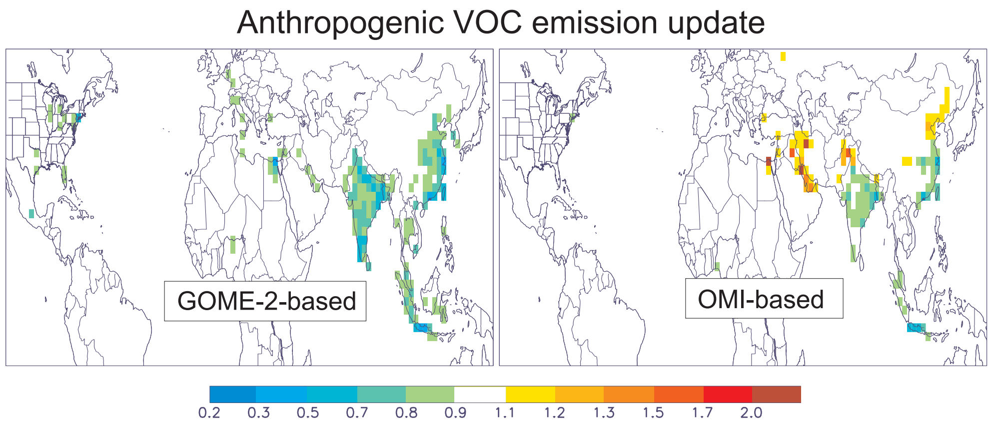

Fig. 11. Same as Fig. 9, but for annual anthropogenic VOC fluxes.

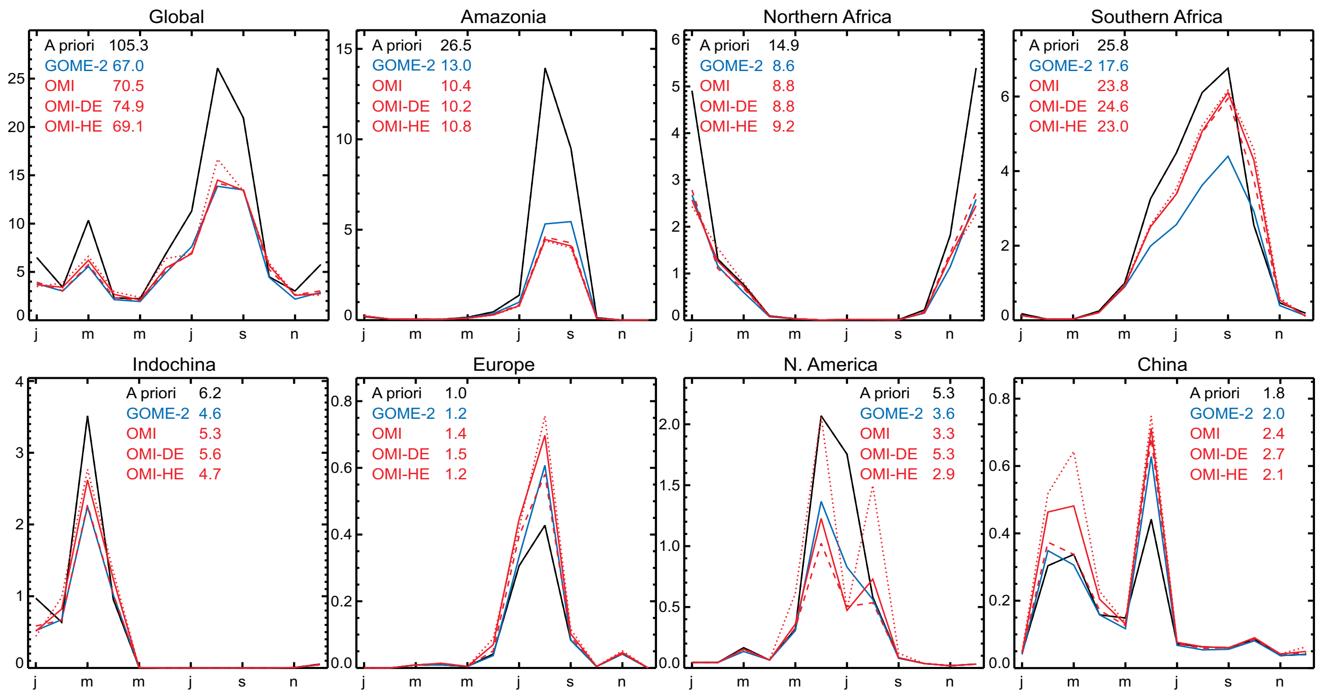

Fig. 12. Monthly variation of a priori and top-down biomass burning VOC fluxes for Amazonia (14°S-10°N, 45-80°W), Africa north and south of the equator, Indochina (6-22°N, 97.5-110°E), Europe (including European Russia), N. America (US and Canada), China, and worldwide, expressed in TgVOC/month. Solid lines are used for the a priori emissions (black), updated emissions inferred from GOME-2 (blue) and OMI (red) observations. Dotted and dashed red lines are used for the results of the sensitivity studies OMI-DE, and OMI-HE (Table 2), respectively. For each inversion annual fluxes for 2010 (in TgVOC) are given inside the panels.

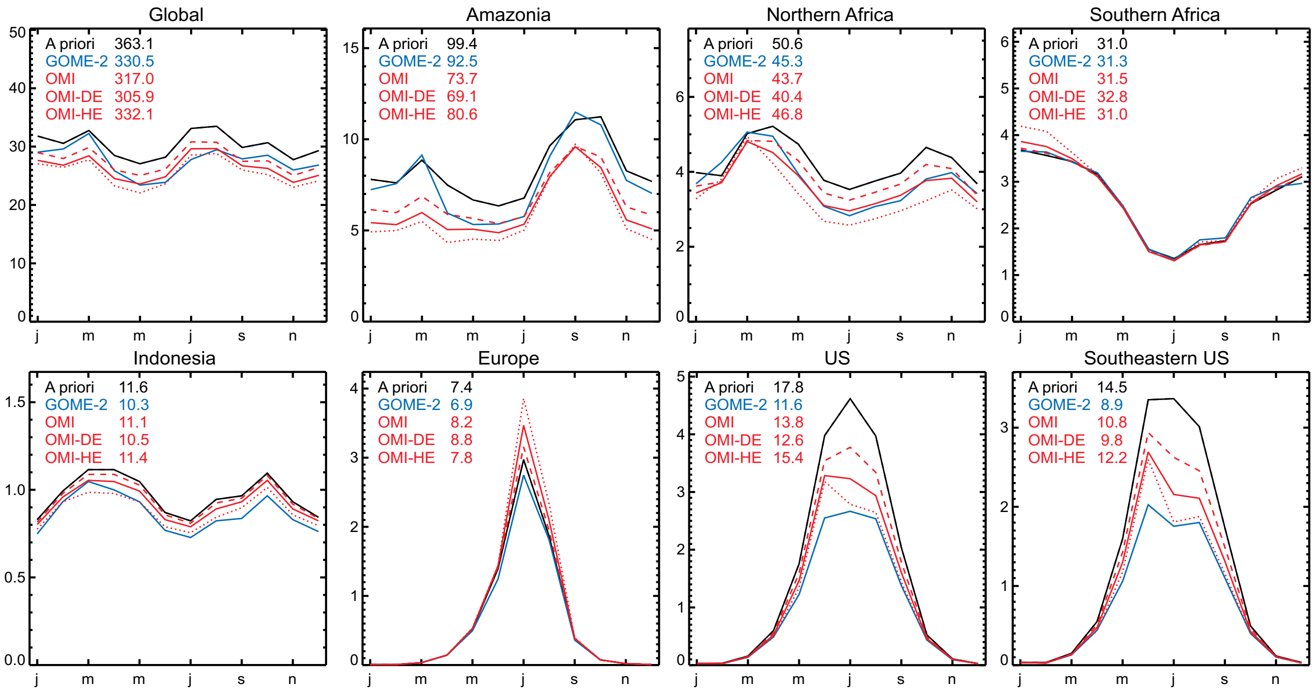

Fig. 13. Monthly variation of a priori and satellite-derived isoprene fluxes for Amazonia, Northern and Southern Africa, Europe, N. America (defined as in Fig. 12), Indonesia (10°S-6°N, 95-142.5°E), and Southeastern US (25-38°N, 60-100°W). The color and line code is the same as in Fig. 12. Units are Tg of isoprene per month. Annual isoprene fluxes per region are given in each panel in Tg of isoprene.

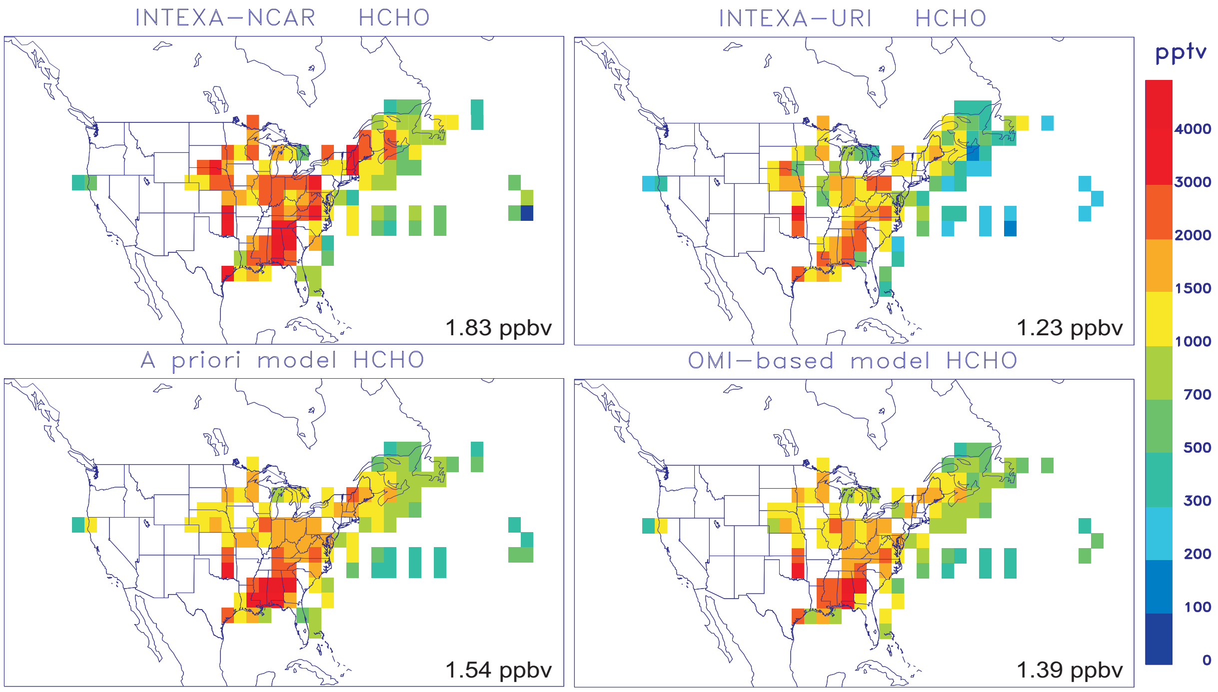

Fig. 14. Comparison between HCHO measurements from the INTEX-A campaign and model concentrations sampled at the measurement times and locations from the a priori simulation and from the OMI-based inversion averaged between the surface and 2 km. The HCHO data are reported from two different instruments, from the National Center for Atmospheric Research (NCAR) and from the University of Rhode Island (URI). The observed and modelled mean HCHO concentrations over the flight domain and altitude range are given inside each panel.

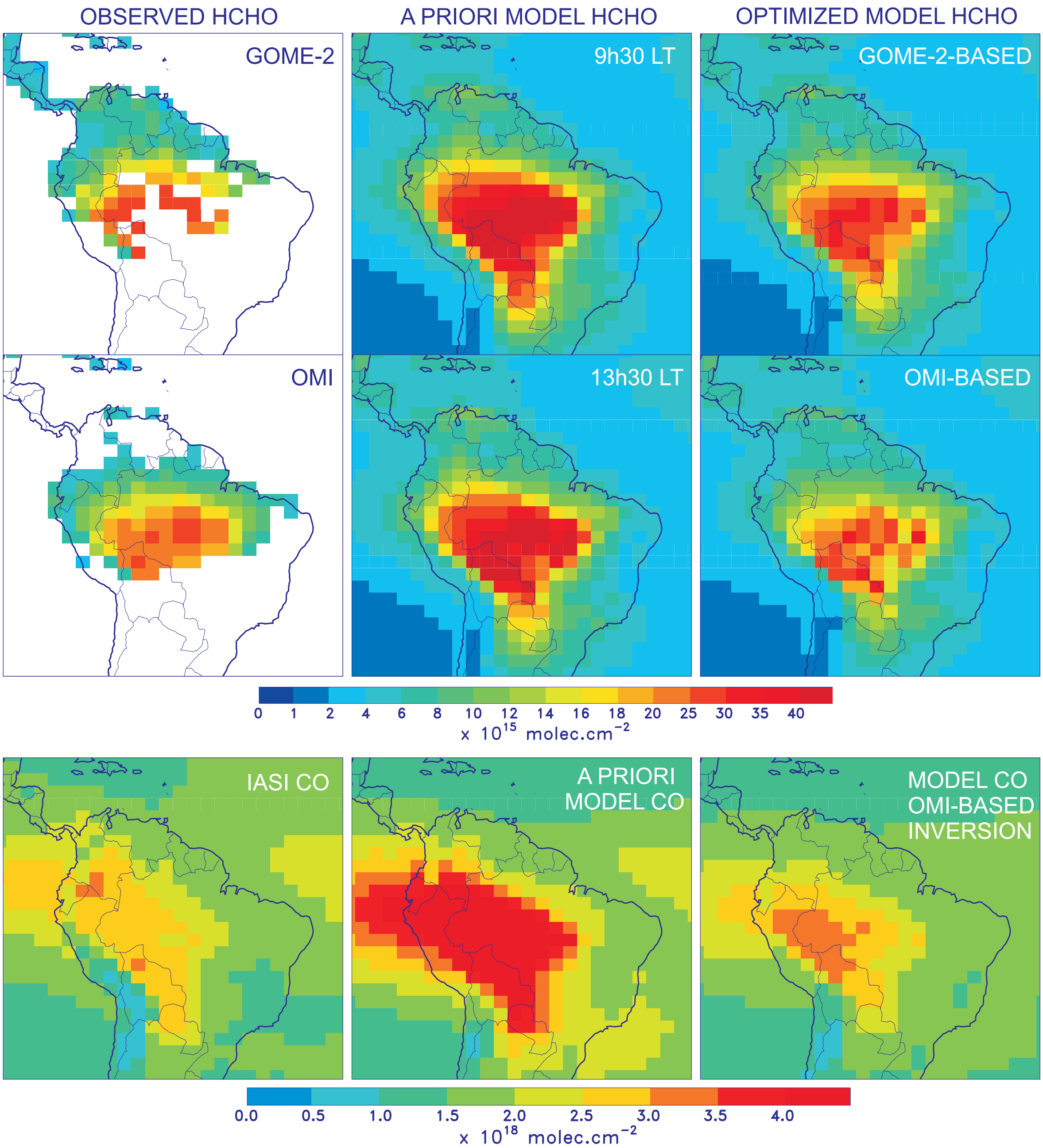

Fig. 15. Observed, a priori and a posteriori model HCHO columns (in 10^{15} molec.cm^{-2}) derived from GOME-2 (upper) and OMI (middle) inversions in Amazonia in August 2010. For the same month, observed CO columns by IASI, a priori model CO columns and CO columns (in 10^{18} molec.cm^{-2}) from the OMI-based inversion are shown in the bottom panels. CO results from the GOME-2 inversion are very similar to those obtained from OMI and are therefore not shown here.

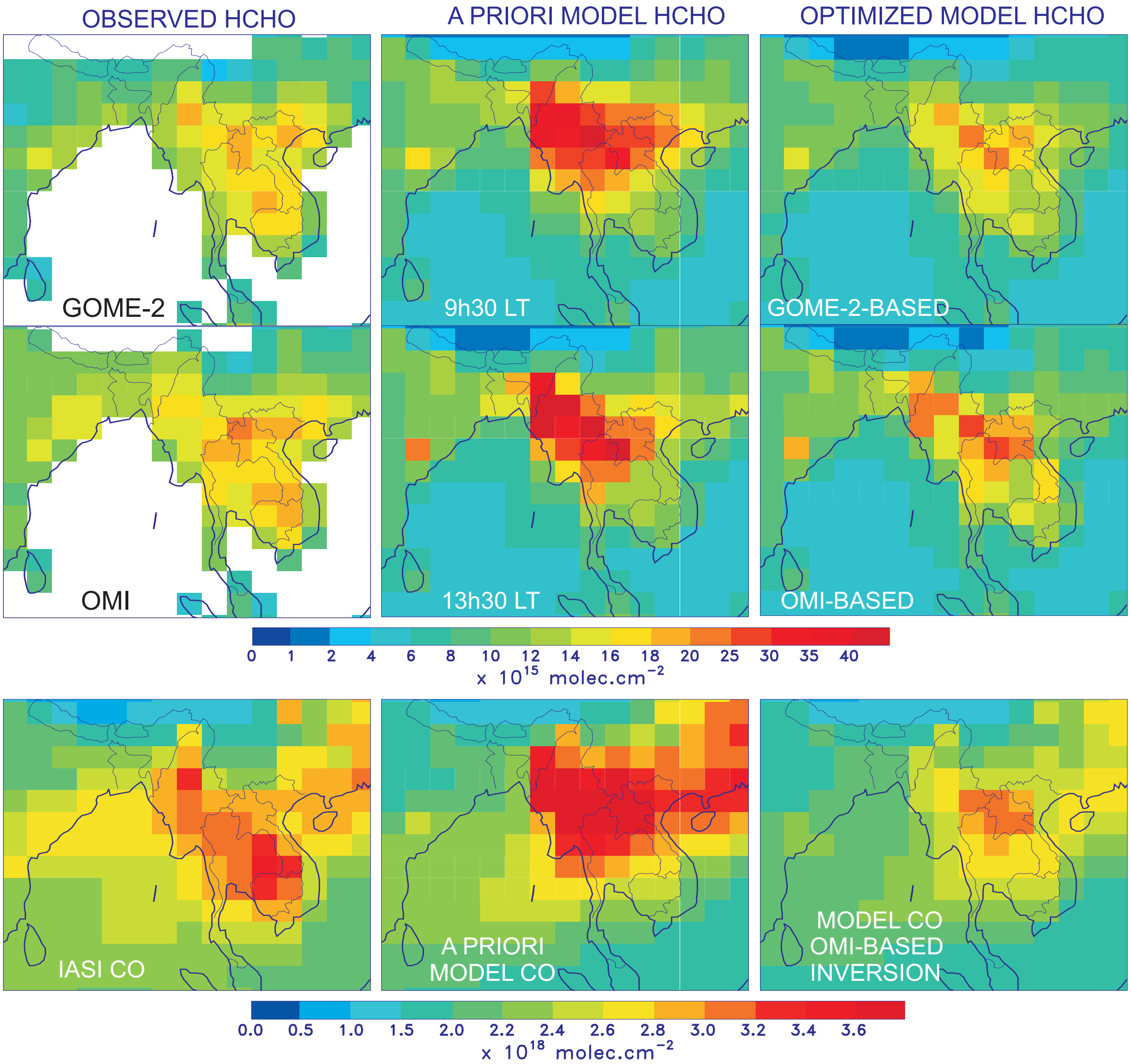

Fig. 16. Same as Fig. 15 for the Indochinese Peninsula in March 2010.